ACSNANO

www.acsnano.org

ARTICLE

High-Throughput *In Vivo* Screening Identifies Differential Influences on mRNA Lipid Nanoparticle Immune Cell Delivery by Administration Route

Alex G. Hamilton, Kelsey L. Swingle, Ajay S. Thatte, Alvin J. Mukalel, Hannah C. Safford, Margaret M. Billingsley, Rakan D. El-Mayta, Xuexiang Han, Benjamin E. Nachod, Ryann A. Joseph, Ann E. Metzloff, and Michael J. Mitchell*

Cite This: https://doi.org/10.1021/acsnano.4c01171

Read Online

ACCESS | Metrics & More | Article Recommendations | Supporting Information

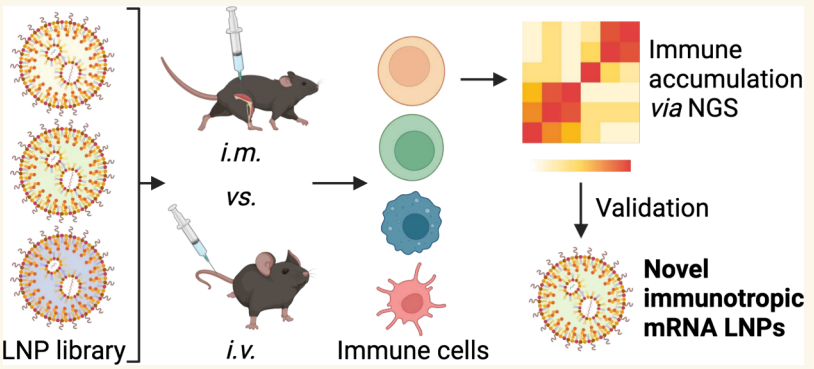

ABSTRACT: **Immune modulation through the intracellular delivery of nucleoside-modified mRNA to immune cells is an attractive approach for *in vivo* immunoengineering, with applications in infectious disease, cancer immunotherapy, and beyond. Lipid nanoparticles (LNPs) have come to the fore as a promising nucleic acid delivery platform, but LNP design criteria remain poorly defined, making the rate-limiting step for LNP discovery the screening process. In this study, we employed high-throughput *in vivo* LNP screening based on molecular barcoding to investigate the influence of LNP composition on immune tropism with applications in vaccines and systemic immunotherapies. Screening a large LNP library under both intramuscular (*i.m.*) and intravenous (*i.v.*) injection, we observed differential influences on LNP uptake by immune populations across the two administration routes, gleaning insight into LNP design criteria for *in vivo* immunoengineering. In validation studies, the lead LNP formulation for *i.m.* administration demonstrated substantial mRNA translation in the spleen and draining lymph nodes with a more favorable biodistribution profile than LNPs formulated with the clinical standard ionizable lipid DLin-MC3-DMA (MC3). The lead LNP formulations for *i.v.* administration displayed potent immune transfection in the spleen and peripheral blood, with one lead LNP demonstrating substantial transfection of splenic dendritic cells and another inducing substantial transfection of circulating monocytes. Altogether, the immunotropic LNPs identified by high-throughput *in vivo* screening demonstrated significant promise for both locally- and systemically-delivered mRNA and confirmed the value of the LNP design criteria gleaned from our screening process, which**

continued...

Received: January 24, 2024
Revised: May 13, 2024
Accepted: May 22, 2024

could potentially inform future endeavors in mRNA vaccine and immunotherapy applications.

KEYWORDS: *lipid nanoparticles, mRNA, in vivo, high-throughput screening, immunoengineering, vaccines*

INTRODUCTION

Immune nucleic acid delivery is an attractive and rapidly growing area of research[1]—nucleic acid delivery-based approaches to immunoengineering have been extensively investigated in prophylactic vaccines, such as vaccines against Ebola virus and SARS-CoV-2,[2−5] and in cancer immunotherapy for cytokine production, neoantigen vaccines, and, more recently, antigen receptor engineering.[6−10] Historically, viral vectors have been used for most nucleic acid delivery applications, including immunoengineering.[1,11] However, viral vectors possess a number of practical shortcomings, such as immunogenicity, limited payload size, poor manufacturing scalability, relatively low transgene copy number, and the risk of insertional mutagenesis and associated genotoxicity.[12−16] Furthermore, retroviral transduction results in permanent phenotypic alterations by virtue of its persistent genome modifications, which can be detrimental when engineering long-lived immune cells and exacerbates concerns associated with side effects and off-target effects.[17,18]

Intracellular delivery of nucleoside-modified mRNA has emerged as a clinically validated alternative to viral transduction for nucleic acid therapy and vaccines.[1−3,11,14,19] However, nucleic acid vaccines and therapeutics face a number of biological and physiological barriers.[20] The foremost barrier is localization: the mRNA cargo must first be transported to the correct tissue and cell types to perform its therapeutic function. For vaccines, lymphoid tissue such as the lymph nodes is typically the desired target, reached by draining from nearby connective tissue, where mRNA should be delivered to antigen-presenting cells (APCs) such as dendritic cells (DCs).[21] For cancer immunotherapies, effector cells in the blood and spleen, accessible by systemic administration into the bloodstream, are often an attractive target.[22−24] However, mRNA must be shielded in transit from degradation by nucleases present in high abundance in serum and immune organs.[25] Upon safely reaching the cells of interest, the properties of mRNA as a large, anionic biomacromolecule further hinder delivery, preventing the nucleic acid from crossing the cell membrane on its own.[11] Once the mRNA enters the cell, it must escape from intracellular vesicles to reach the cytoplasm without being degraded, where it can finally be translated to the desired therapeutic protein.[26,27]

Lipid nanoparticles (LNPs) have gained traction in recent years as a promising nonviral delivery vehicle for a variety of nucleic acids, including plasmid DNA (pDNA), single-stranded DNA (ssDNA), small interfering RNA (siRNA), and mRNA.[20,28−32] The principal lipid component of interest in LNPs is a pH-responsive ionizable lipid, which responds to acidification of the endosome by protonating, leading to the disruption of the endosomal membrane and release of cargo into the cytoplasm.[33] LNPs also commonly contain three additional excipients that play important roles in the function of the LNP: cholesterol, crucial for membrane stability and fusion; helper phospholipids, which assist in coordination with the nucleic acid cargo and membrane formation; and a lipid-anchored polyethylene glycol (PEG) or equivalent, which sterically hinders interactions with cells and extracellular matrix, prolonging LNP circulation time and decreasing immune interactions.[34] While LNPs are capable of extremely potent liver transfection under systemic administration due to a first-pass effect, extrahepatic delivery remains an area of significant active research.[35,36] It is well-known that differences in LNP chemistry can result in differential cellular uptake, leading to a cellular tropism.[35,37] This cell type-selectivity is attractive for immunoengineering applications, where some applications (*e.g.*, vaccines) require nucleic acid delivery to APCs and others (*e.g.*, cancer immunotherapy) are largely based on delivery to effector cells.[22,27,38,39] New ionizable lipid structures have been extensively studied as a means to alter LNP performance and tropism.[31,40−44] Furthermore, several studies have shown that simple modification of the molar composition of the lipid components can influence delivery profiles *in vivo* and *ex vivo*.[32,45−47]

While advances have been made in the understanding of LNP structure−function relationships, the development of LNPs remains largely driven by discovery rather than rational design.[35,48] This screening-based discovery process is historically relatively low-throughput, often relying on techniques such as luminescence imaging with reporter genes (*e.g.*, firefly luciferase, FLuc) or other singleplex measurements.[40,43,49,50] However, our group and others have reported the adaptation of next-generation sequencing (NGS) to multiplex the *in vivo* screening of LNPs, greatly increasing the throughput of the discovery process.[51−54] In these methods, dozens of LNP formulations are prepared, each encapsulating a nucleic acid cargo with a distinct polymorphic barcode sequence. These LNPs can then be combined and injected as a pool, and NGS can be used to quantify the relative abundance of each LNP formulation in the samples of interest (Figure 1a).

The present study sought to use high-throughput screening to investigate the influence of LNP composition on uptake by distinct immune cell populations with potential applications in vaccine development and cancer immunotherapy. As LNP-mediated RNA delivery to the liver is relatively well-established,[35,45,55−59] we focused our investigation on engineering immune cells in extrahepatic tissues. To this end, we used molecular barcoding and NGS to screen a library of 75 LNPs for delivery to B cells, T cells, DCs, and macrophages/monocytes in the blood, spleen, and draining lymph nodes (Figure 1b). We performed this screen for both *i.m.* and *i.v.* administration routes, using the data collected to elucidate differential compositional factors influencing LNP tropism for each injection route. Notably, we discovered that ionizable lipid structure was a key determinant of LNP performance under systemic administration, likely due to its influence on protein corona formation, while lipid excipient composition appeared to strongly influence LNP fate under local administration, perhaps due to changes in LNP physicochemical properties. We then validated promising LNP formulations identified by this screening in isolation using low-throughput screening to confirm immune tropisms, demonstrating substantial immune cell uptake and transfection with our lead LNP formulations. The LNP formulations identified in this study hold promise for immunoengineering applications based on modified mRNA and demonstrate the value of the design criteria developed through high-throughput *in vivo* screening.

https://doi.org/10.1021/acsnano.4c01171
ACS Nano XXXX, XXX, XXX−XXX

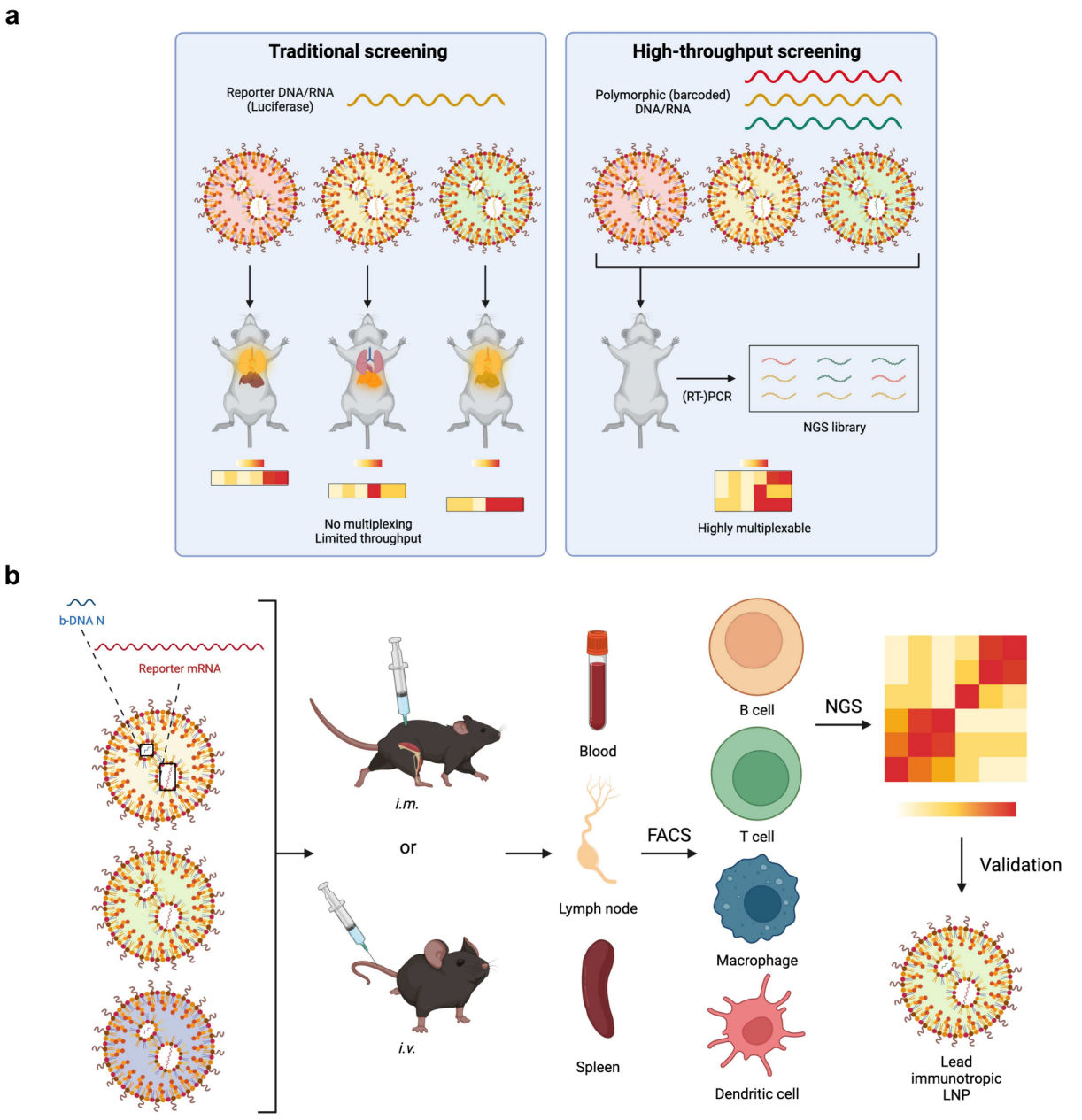

Figure 1. High-throughput screening using molecular barcoding enables *in vivo* evaluation of mRNA LNP formulations for immune tropism. (a) Comparison of traditional mRNA LNP screening using reporter genes *vs* high-throughput *in vivo* mRNA LNP screening using molecular barcoding. Traditional screening using reporter genes is typically singleplex, while molecular barcoding massively increases screening throughput through multiplexing. (b) Overview of high-throughput screening approach used to develop immunotropic mRNA LNPs. A library of 75 LNPs encapsulating reporter mRNA along with barcoded DNA (b-DNA) was formulated and administered to healthy mice *via* either *i.m.* or *i.v.* administration. Peripheral blood, inguinal lymph nodes, and spleens were isolated as immune tissues of interest, and immune cells were isolated from each using fluorescence-activated cell sorting (FACS). High-throughput screening methodologies based on next-generation sequencing (NGS) were employed to identify key parameters influencing LNP performance and lead candidates for each administration route, identifying a complex dependence on lipid excipient composition for *i.m.* administration and a dependence on ionizable lipid structure for *i.v.* administration. These lead candidates were then validated in isolation to evaluate their potential for *in vivo* immunoengineering using mRNA.

RESULTS AND DISCUSSION

High-Throughput Screening of LNP Composition for *In Vivo* Immune Cell Delivery. To probe the effects of the lipid identity and relative composition on LNP uptake in immune cells, we formulated a library of 75 LNPs. Each LNP consisted of four lipid components—an ionizable lipid, 1,2-dioleoyl-*sn*-glycero-3-phosphoethanolamine (DOPE), cholesterol, and lipid-PEG (C14-PEG2000)—and mRNA encoding the monomeric red fluorescent protein mCherry along with a barcoded DNA oligomer (b-DNA) uniquely identifying the LNP formulation (Table S1). The library consisted of two portions: one dedicated to probing the effects of ionizable lipid structure and one dedicated to investigating varying lipid molar ratios (Table S2). To investigate ionizable lipid structure, excipient molar compositions were held fixed based on previously identified LNP formulations for mRNA delivery and the identity of the ionizable lipid was changed to produce 27 distinct LNP formulations (Figure S1).[45] For excipient molar

https://doi.org/10.1021/acsnano.4c01171
ACS Nano XXXX, XXX, XXX−XXX

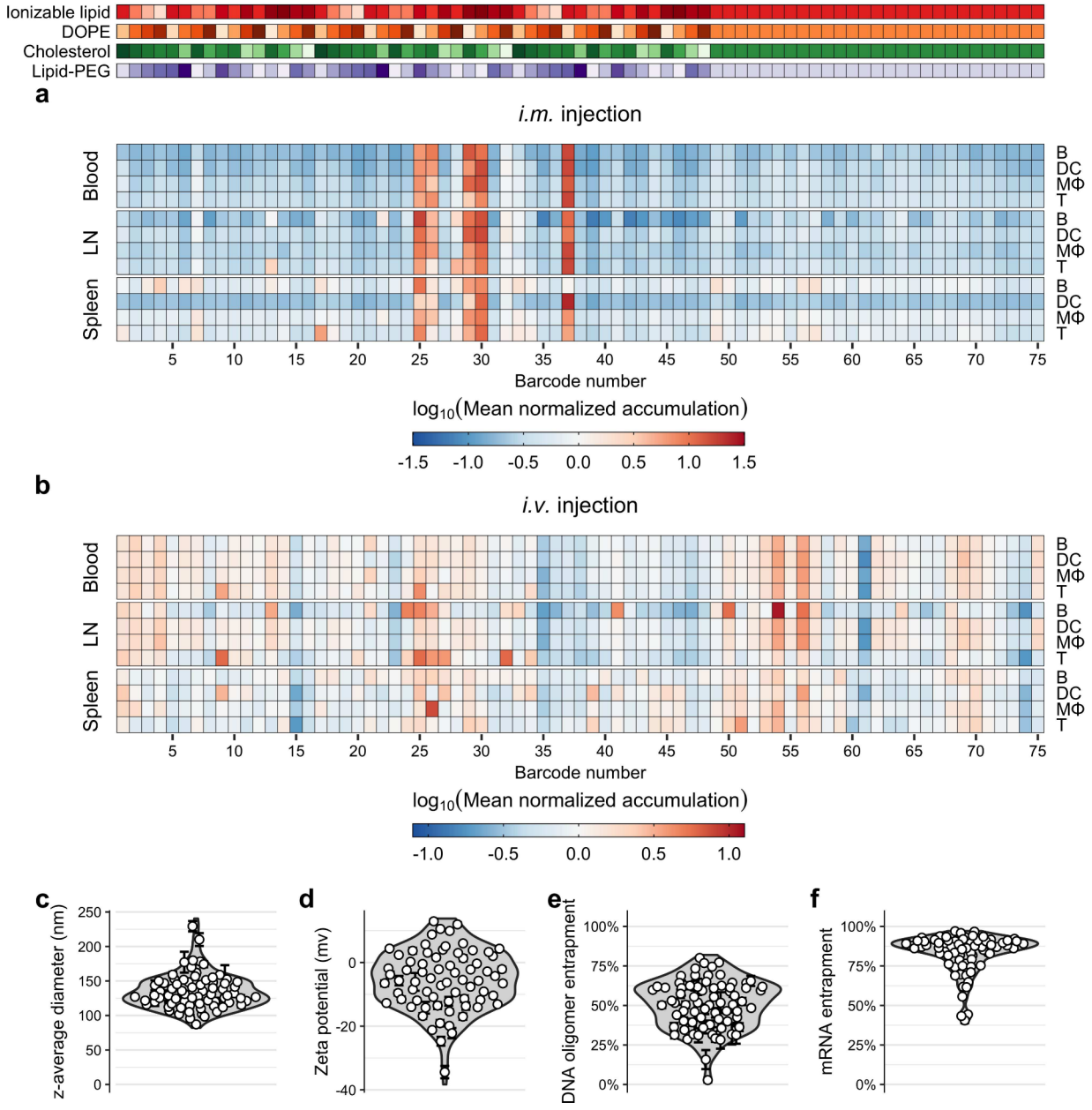

Figure 2. High-throughput *in vivo* screening suggests differential factors influencing mRNA LNP uptake by immune cells across injection routes. (a, b) Heatmaps depicting relative intracellular accumulation of each LNP formulation within each sample as quantified by next-generation sequencing for *i.m.* (a) and *i.v.* (b) administration. Lower normalized values (blue) indicate depletion of a b-DNA relative to the library pool, while greater values (red) indicate enrichment. Data are presented as mean values from $n = 4$ independent biological replicates. B: B cells. DC: dendritic cells. MΦ: macrophages/monocytes. T: T cells. LN: lymph nodes. (c–f) Violin plots characterizing the formulated LNP library on the basis of hydrodynamic diameter (c), zeta potential (d), b-DNA entrapment (e), and mRNA entrapment (f). Each point represents a distinct LNP formulation. Characterization data are presented as mean ± standard error of the mean ($n \geq 3$ independent observations).

composition screening, we employed an orthogonal design-of-experiments approach (Taguchi $L_{16}(4^4)$) for each of the three ionizable lipids (C12–200, C14–494, and C16–488), resulting in 48 additional LNP formulations.

We produced LNPs *via* microfluidic mixing as described previously,[43] then characterized all LNPs on the basis of size, charge, and encapsulation of both mRNA and b-DNA. Characterization showed that most formulated LNPs were between 100 and 150 nm in diameter (Figure 2c), with most formulations demonstrating efficient mRNA encapsulation with over 75% mean entrapment (Figure 2f). b-DNA encapsulation was notably lower than mRNA encapsulation, likely due to the smaller size of b-DNA oligomers; however, most LNPs demonstrated at least 50% b-DNA entrapment and nearly all displayed at least 25% entrapment, easily sufficient for NGS-based screening (Figure 2e), especially as previous studies have demonstrated that free b-DNA does not substantially accumulate in tissues.[53,60] We postulate that the presence of unencapsulated b-DNA likely contributes to the slightly negative zeta potential measurements observed (Figure 2d). After confirming appropriate physicochemical parameters, we combined all LNPs into a single injection pool. We administered this injection pool to $n = 4$ C57BL/6 mice *via* either *i.m.* or *i.v.* injection, allowed LNPs to distribute and enter cells, and then

https://doi.org/10.1021/acsnano.4c01171
ACS Nano XXXX, XXX, XXX–XXX

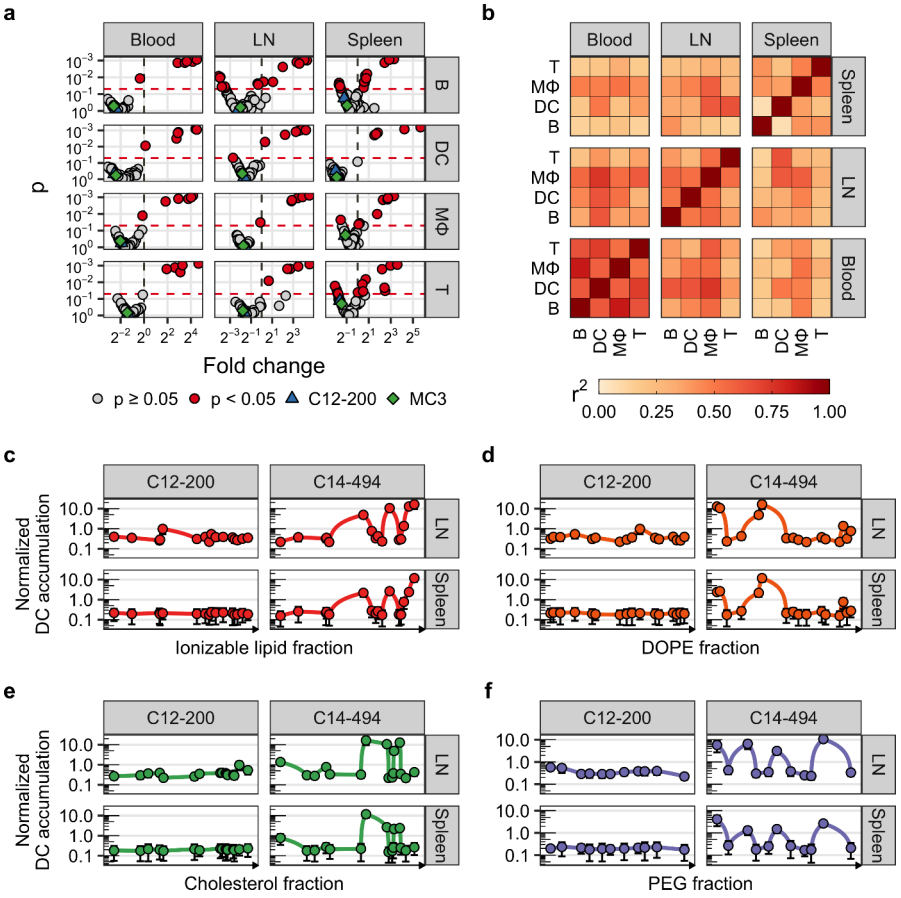

Figure 3. LNP excipient molar composition strongly influences immune cell uptake following *i.m.* administration. (a) Relative enrichment of barcodes within each analyzed cell population following *i.m.* injection. Fold change is presented relative to the aggregate LNP pool (*i.e.*, basemean). LNPs formulated using C12−200 and MC3 ionizable lipids are highlighted as controls. $\alpha = 0.05$ is indicated as a dashed horizontal line: points above this line (red) are either significantly enriched (top right) or depleted (top left). Points below this line (gray) do not demonstrate significantly different uptake from the aggregate LNP pool. (b) Squared pairwise Pearson correlation (r^2) for LNP uptake in each pair of samples following *i.m.* injection. (c−f) Normalized accumulation in dendritic cells (DCs) from spleens and draining lymph nodes (LN) *vs* ionizable lipid fraction (c), DOPE fraction (d), cholesterol fraction (e), and PEG fraction (f) for C12−200 and C14−494 ionizable lipids following *i.m.* administration. Data are presented as mean ± standard error of the mean for $n = 4$ independent biological replicates. B: B cells. MΦ: macrophages/monocytes. T: T cells.

sacrificed mice and collected peripheral blood, spleens, and inguinal lymph nodes (Figure 1b). After obtaining single-cell suspensions from collected samples, we used fluorescence-activated cell sorting (FACS) to isolate B cells, T cells, DCs, and macrophages/monocytes from each sample. We then lysed and digested sorted cells to isolate b-DNA and amplified barcoded oligomers using polymerase chain reaction (PCR) with overhanging primers designed to add sequencing adapters and indices (Table S3). We combined the resultant NGS libraries to create a library pool, which we sequenced to quantify LNP uptake in each sample. The main quantity derived from NGS data is normalized intracellular accumulation, which is calculated as the ratio of read fraction in collected samples (output) to read fraction in the administered LNP pool (input). This quantity summarizes the relative intracellular accumulation of each LNP within a sample.

High-Throughput *In Vivo* Screening Suggests Differential Factors Influencing LNP Performance across Administration Routes. Analysis of NGS data (Figure 2a-b) showed a relatively low hit rate for *i.m.* administration, with the majority of the corresponding accumulation heatmap (Figure 2a) reflecting a mean normalized accumulation less than 1; however, the standouts that did appear demonstrated a relatively high mean normalized accumulation. Interestingly, the apparent hits on the heatmap fell within the portion of the LNP library dedicated to excipient composition screening, suggesting that relative molar composition of the lipid components of the LNP may be important in determining LNP fate under *i.m.* administration, perhaps due to changes in LNP physicochemical characteristics. Conversely, *i.v.* injection demonstrated a relatively high hit rate, but there were fewer standouts in normalized accumulation: most of the heatmap was fairly unsaturated, suggesting relatively low magnitudes of normalized accumulation (Figure 2b). Furthermore, the portion of the library dedicated to ionizable lipid screening appeared less homogeneous than that dedicated to excipient composition, suggesting that relative molar composition may have less of an effect for *i.v.* administration and that ionizable lipid identity might be more important for immune cell uptake, perhaps due to changes in protein corona formation.[61−63] These results bring to attention the importance of the administration route as a factor to consider for LNP design. Because of the observed differences in the two administration routes, we further analyzed the NGS data for the two separately.

Molar Composition of LNP Lipid Excipients Strongly Influences Immune Uptake under Intramuscular Adminis-

https://doi.org/10.1021/acsnano.4c01171
ACS Nano XXXX, XXX, XXX−XXX

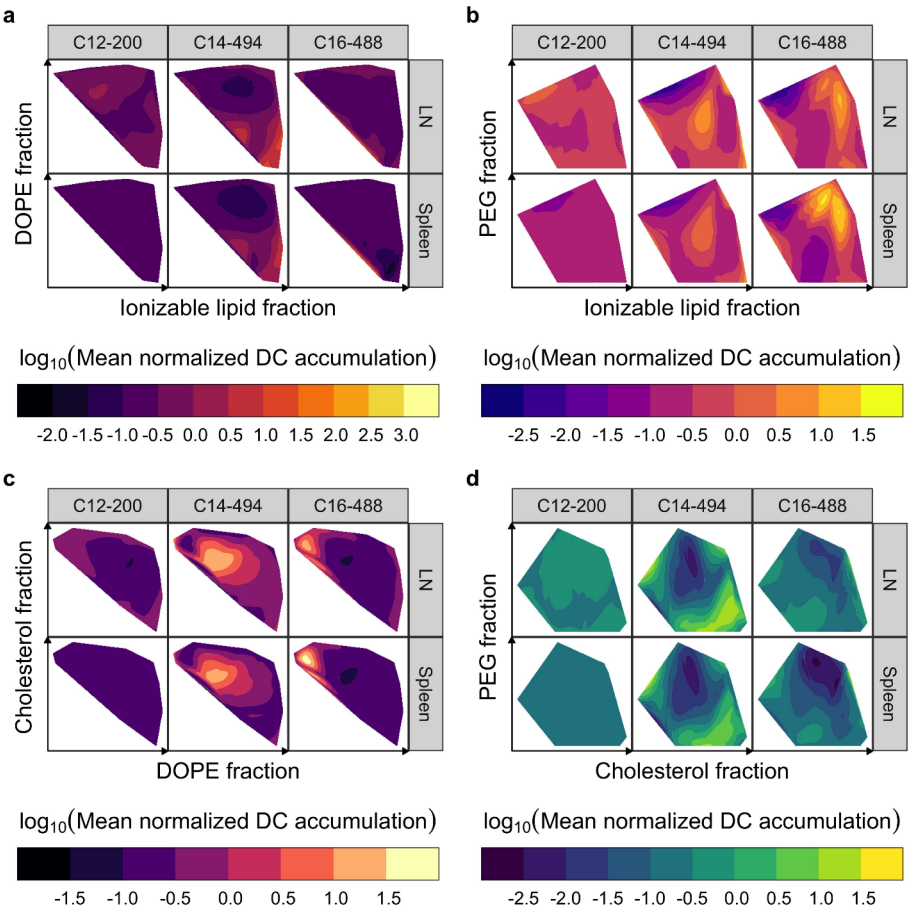

Figure 4. Ionizable lipid structure and excipient composition demonstrate synergistic influences on LNP performance under *i.m.* administration. (a–d) Mean normalized LNP dendritic cell (DC) accumulation in spleens and draining lymph nodes (LN) *vs* DOPE and ionizable lipid fractions (a), PEG and ionizable lipid fractions (b), cholesterol and DOPE fractions (c), and PEG and cholesterol fractions (d) for C12–200, C14–494, and C16–488 ionizable lipids following *i.m.* administration. Lighter regions indicate local maxima in LNP uptake by DCs. Data are interpolated from the mean of $n = 4$ independent biological replicates.

tration. To more clearly understand the relative performance of LNP formulations within each sample, we compared the normalized accumulation of each formulation against that of all other formulations using the Wilcoxon rank-sum test. This enrichment analysis enables the quantification and inferential analysis of the relative performance of LNP formulations. Resultant volcano plots showed a handful of highly enriched LNP formulations and a large cluster of slightly depleted formulations in most cases (Figure 3a). In some cases (*e.g.*, splenic lymphocytes), a small number of these depleted LNPs were significantly depleted compared to the aggregate, but enrichment analysis largely suggested a small number of standout LNPs and little difference in uptake among the remaining LNPs under *i.m.* administration. To complement volcano plots and investigate the degree of specificity observed—*e.g.*, whether LNPs that delivered well to one cell type within a particular organ delivered well to other cell types within that organ—we also calculated and plotted squared Pearson correlation coefficients r^2 between normalized accumulation profiles for each pair of samples following *i.m.* injection (Figure 3b). Under *i.m.* injection, all cell types in the blood showed a relatively high coefficient of determination in uptake compared to other blood cell types, but we observed little other similarity beyond perhaps a slight correlation between samples in the blood and lymph nodes. These findings suggest that those LNP formulations that were able to reach circulation may have entered cells in the bloodstream with low specificity, but that LNPs that remained in the lymph nodes may have preferentially entered particular cell types based on LNP physicochemical characteristics.

Ionizable Lipid Structure Determines How Excipient Composition Influences LNP Performance Following Intramuscular Administration. To investigate the impact of excipient composition on LNP fate following *i.m.* injection, we examined the influence of the proportional amount of each lipid component on accumulation for each sample using 1D (no interaction) and 2D (including interaction) analyses. In general, one-dimensional analysis suggested that a moderate-to-high ionizable lipid content was beneficial for immune cell uptake in all organs, with relatively low DOPE content and relatively high cholesterol and PEG fractions being preferred (Figure 3c-f). Interestingly, we found that there was very little difference in uptake for LNPs formulated using C12–200 regardless of excipient composition. We focused instead on those LNPs formulated using the ionizable lipids C14–494 ("C14–4") and C16–488 ("C16–2"), previously reported by our group to be suitable for the transfection of immune cells *in vitro* and *ex vivo*.[43] Higher-order effects (*i.e.*, second-order and higher) are thought to be important for understanding structure–function relationships of LNPs.[45] We therefore turned our attention to two-dimensional relationships. Here, we noticed that the two ionizable lipids that showed noticeable differences in delivery

https://doi.org/10.1021/acsnano.4c01171
ACS Nano XXXX, XXX, XXX–XXX

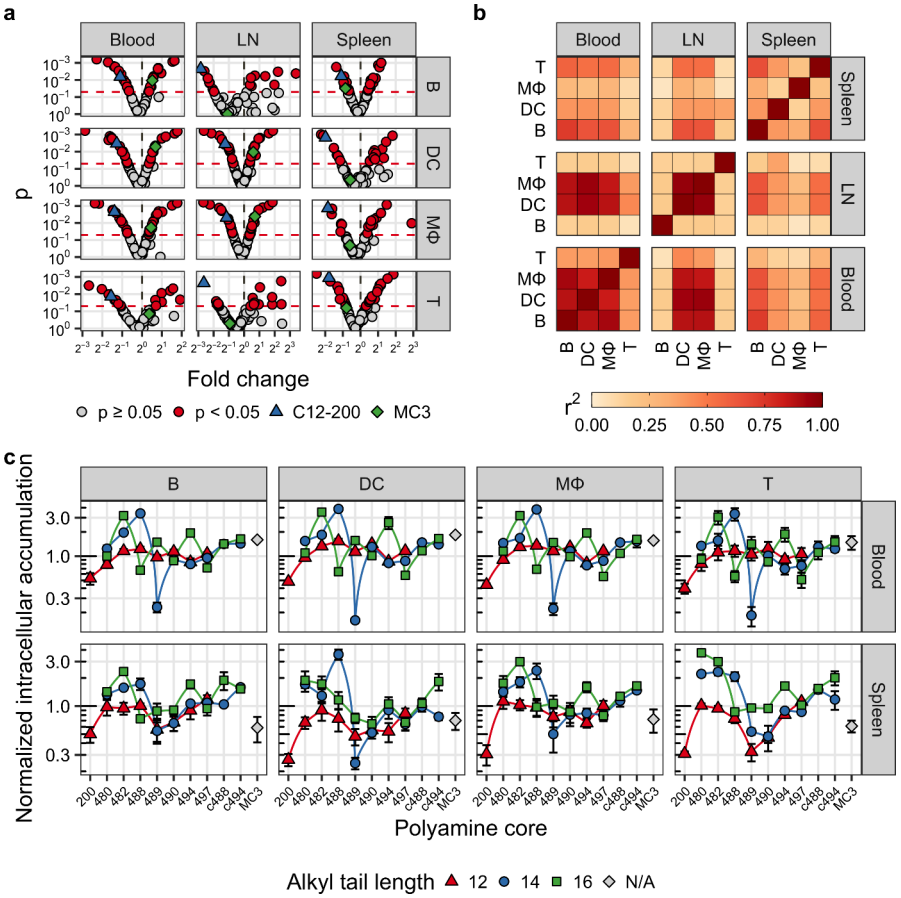

Figure 5. High-throughput *in vivo* screening identifies promising LNP candidates for immune cell uptake under systemic administration. (a) Relative enrichment of barcodes within each analyzed cell population following *i.v.* injection. Fold change is presented relative to the aggregate LNP pool (*i.e.*, basemean). LNPs formulated using C12−200 and MC3 ionizable lipids are highlighted as controls. $\alpha = 0.05$ is indicated as a dashed horizontal line: points above this line (red) are either significantly enriched (top right) or depleted (top left). Points below this line (gray) do not demonstrate significantly different uptake from the aggregate LNP pool. (b) Squared pairwise Pearson correlation (r^2) for LNP uptake in each pair of samples following *i.v.* injection. (c) Normalized accumulation by polyamine core structure and alkyl epoxide tail length following *i.v.* injection. Ionizable lipids were synthesized by addition of alkyl-terminated epoxides containing 12, 14, or 16 carbons to the indicated polyamine cores. LNPs formulated using C12−200 and MC3 ionizable lipids are included as positive controls. Data are presented as mean ± standard error of the mean from $n = 4$ independent biological replicates. B: B cells. DC: dendritic cells. MΦ: macrophages/monocytes. T: T cells. LN: lymph nodes.

influenced by lipid composition—C14−494 and C16−488—displayed somewhat different trends in delivery (Figure 4). For instance, while a high ionizable lipid fraction and low DOPE fraction appear beneficial for C14−494, the same does not appear to hold true for C16−488 (Figure 4a). Similarly, there is a clear local maximum in normalized accumulation for moderate levels of ionizable lipid and PEG for C14−494, while this maximum is less well-defined and somewhat shifted for C16−488 (Figure 4b). Interestingly, when investigating the joint effects of cholesterol and DOPE fractions on delivery, we noticed that low DOPE combined with high cholesterol levels appeared to be beneficial for delivery using C16−488 (Figure 4c). However, the corresponding composition for C14−494 showed depletion rather than enrichment, demonstrating a notable difference between the two ionizable lipids. Furthermore, it appears that relatively low PEG and high cholesterol content led to high delivery for C14−494, while a lower cholesterol content may have been better for C16−488 (Figure 4d). All told, the two ionizable lipids that displayed composition-dependent delivery effects had notably distinct distributions from each other in most cases, likely due to structural differences between the relatively small 494 polyamine core and the sterically bulkier 488 core. While this analysis did not yield any apparent formulation parameters to gain appreciable specificity of delivery (*i.e.*, plots for distinct tissue/cell type combinations looked largely similar within a given ionizable lipid), these results hint at the importance of ionizable lipid structure as a key consideration for LNP design synergistic with excipient composition for *i.m.* injection.

High-Throughput In Vivo screening Identifies Promising LNP Formulations for Immune Uptake under Intravenous Administration. Enrichment analysis of *i.v.*-injected LNPs identified numerous LNP formulations demonstrating both enrichment and depletion in all samples analyzed (Figure 5a). B cells, DCs, and monocytes in the blood showed fairly high intercorrelation of normalized accumulation under *i.v.* administration, while circulating T cells seemingly displayed a more distinct uptake profile (Figure 5b). Relatively little cross-tissue correlation was observed in samples derived from the spleen and lymph nodes, suggesting the broad transfection of circulating leukocytes. Collectively, these results suggest relatively little diversity in uptake profiles across cell populations under *i.v.*

https://doi.org/10.1021/acsnano.4c01171
ACS Nano XXXX, XXX, XXX−XXX

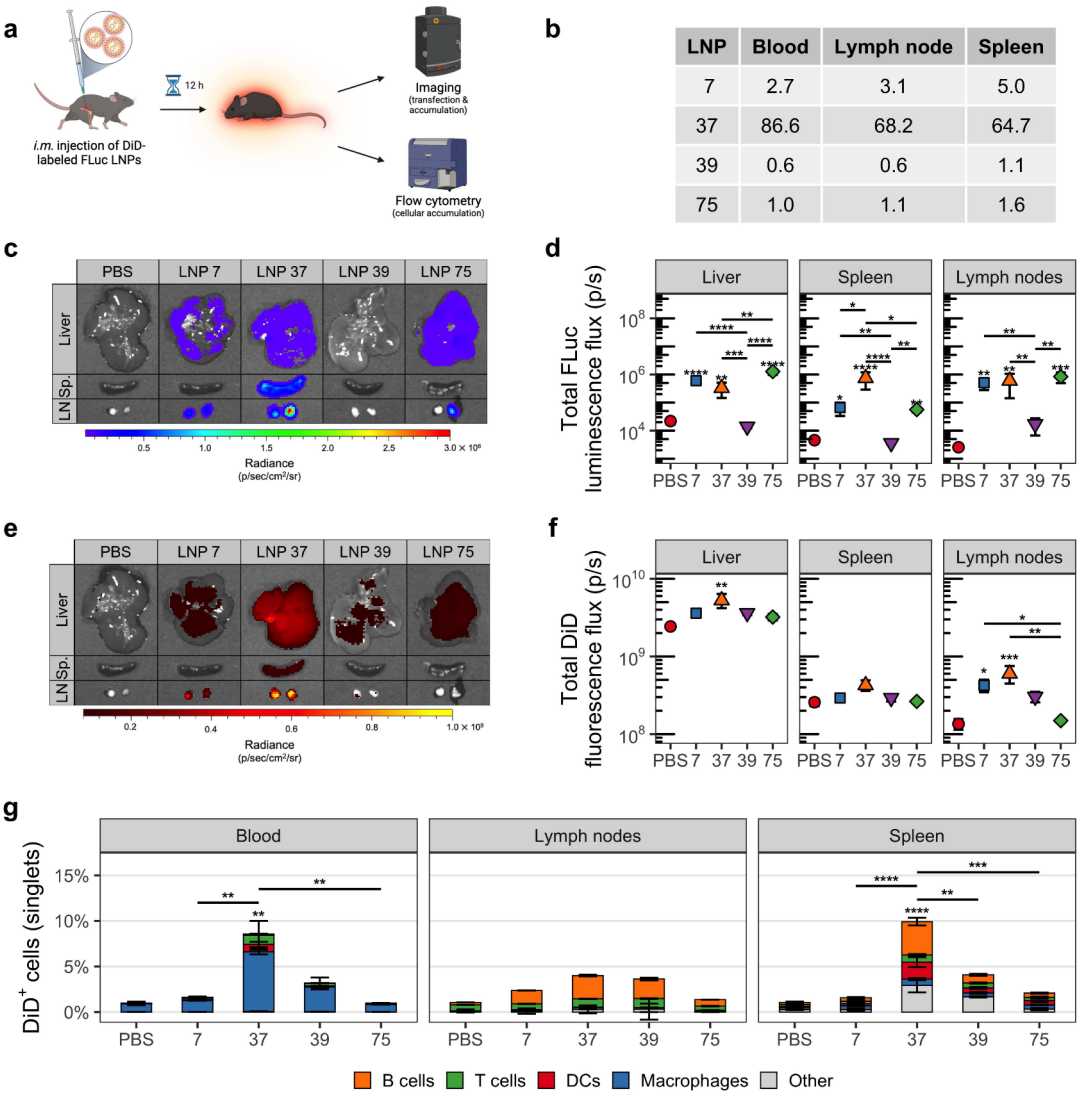

Figure 6. Validation experiments demonstrate the utility of lead LNP candidates for potential *in vivo* immunoengineering applications using local administration. (a) Schematic overview of validation study to assess the immunoengineering potential of LNPs identified by high-throughput *in vivo* screening. LNPs from screening under *i.m.* administration were reformulated encapsulating FLuc mRNA and labeled with the DiD lipophilic fluorescent dye. Twelve hours following injection, mice were sacrificed and organs were subjected to bioluminescence and fluorescence imaging to assess gross LNP accumulation and transfection. Draining lymph nodes, spleens, and peripheral blood were further processed for flow cytometric analysis of intracellular LNP accumulation. (b) Summary of high-throughput screening enrichment analysis describing relative performance of LNP formulations tested in validation studies. Mean enrichment for all cell types was summed for each immune tissue to establish total enrichment. LNP 75 is formulated with the clinical standard MC3 ionizable lipid. (c) Representative *in vivo* imaging system (IVIS) images illustrating FLuc transfection following *i.m.* injection. (d) Region of interest (ROI) quantification of luminescence imaging in validation study. (e) Representative IVIS images illustrating DiD-labeled LNP accumulation following *i.m.* injection. (f) ROI quantification of fluorescence imaging in validation study. (g) Summary data from flow cytometric analysis of peripheral blood, spleens, and lymph nodes following *i.m.* administration of DiD-labeled LNPs. Each stack of bars sums to the fraction of singlets classified as DiD$^+$ and is further stratified into distinct cell types. Statistical annotations above stacked bars indicate comparisons of total DiD positivity rates in singlets. *: $p < 0.05$. **: $p < 0.01$. ***: $p < 0.001$. ****: $p < 0.0001$. Statistical annotations without bars indicate comparisons to PBS. Data are presented as mean ± standard error of the mean for $5 \leq n \leq 7$ independent biological replicates.

administration compared to *i.m.* administration, consistent with systemic distribution *via* the bloodstream.

Ionizable Lipid Structure is a Primary Determinant of Immune Uptake of LNPs Following Systemic Administration. To better understand the impact of ionizable lipid structure on delivery to different immune cell populations, we separated ionizable lipid identity into the two components of the lipid: polyamine core and alkyl epoxide carbon number. We then analyzed the influences of these two variables and their interaction on normalized accumulation (Figure 5c). We observed that mean accumulation in splenocytes was generally higher for the ionizable lipids derived from the longer 16-carbon alkyl epoxide tails than for the respective 12-carbon or 14-carbon versions and that the 12-carbon version, where present, often had the lowest mean accumulation of the set. We also noted that longer alkyl tails generally showed a higher mean delivery in blood and lymph node samples, though less strikingly so. We think that these effects may be due to increased stability of LNPs containing longer alkyl tails in circulation, allowing for a greater duration of immune interaction and trafficking to immune-rich

https://doi.org/10.1021/acsnano.4c01171
ACS Nano XXXX, XXX, XXX−XXX

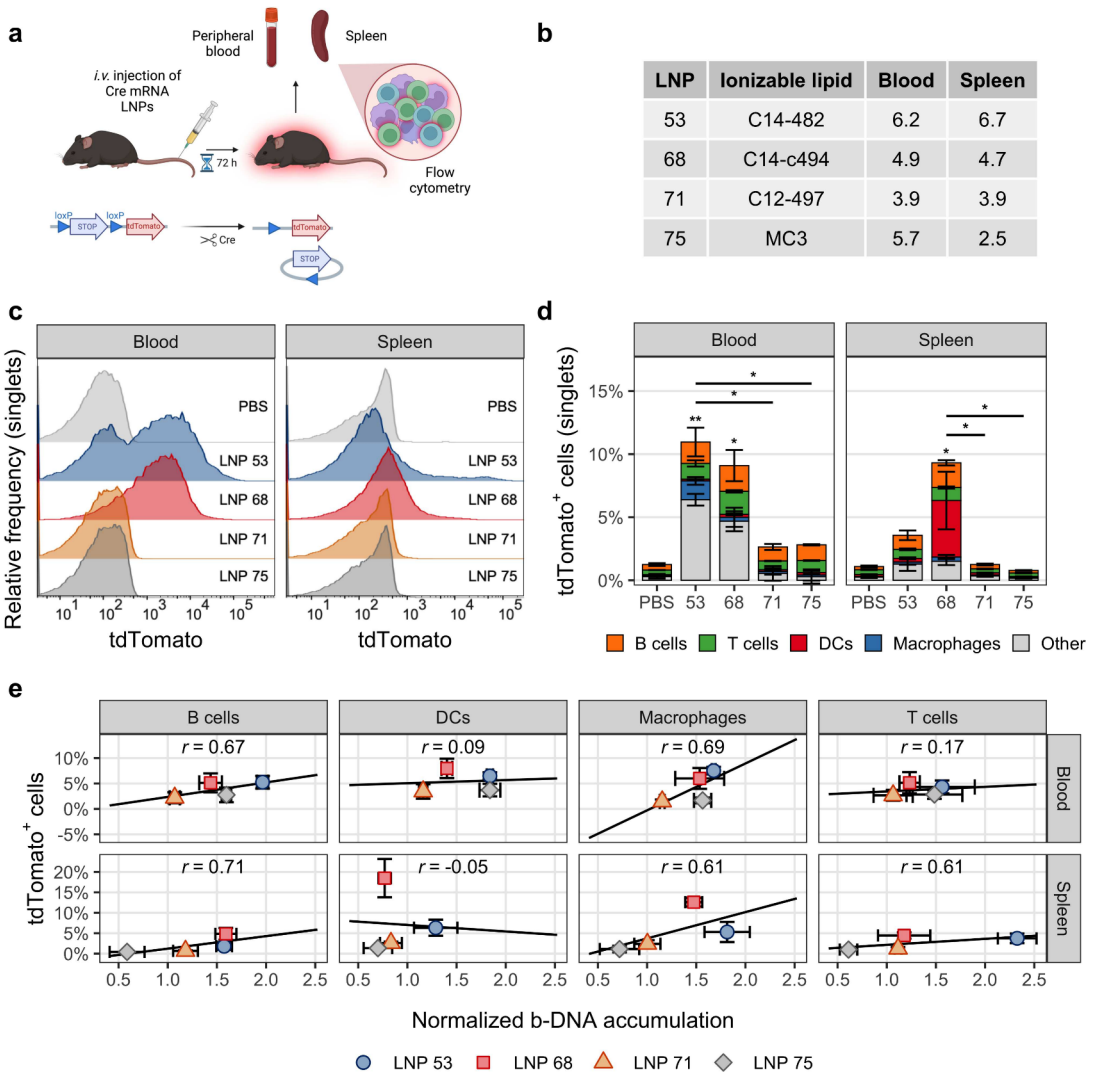

LNP	Ionizable lipid	Blood	Spleen
53	C14-482	6.2	6.7
68	C14-c494	4.9	4.7
71	C12-497	3.9	3.9
75	MC3	5.7	2.5

Figure 7. Validation experiments demonstrate the potency of lead LNP candidates for extrahepatic *in vivo* immunoengineering. (a) Schematic overview of validation study to confirm the systemic immunoengineering potential of LNPs identified by high-throughput *in vivo* screening. LNPs from screening under *i.v.* administration were reformulated encapsulating Cre recombinase mRNA and administered systemically to Ai9 (CAG-loxP-STOP-loxP-tdTomato) mice. 72 h following injection, mice were sacrificed and spleens and peripheral blood were processed for flow cytometric analysis of Cre mRNA transfection. (b) Summary of high-throughput screening enrichment analysis describing relative performance of LNP formulations tested in validation studies. Mean enrichment for all cell types (B cells, T cells, dendritic cells (DCs), and monocytes/macrophages) was summed for both immune tissues (blood and spleen) to establish total enrichment. The ionizable lipid used for each LNP formulation is also listed. (c) Representative histograms from flow cytometric analysis of spleens and peripheral blood following *i.v.* administration of Cre LNPs. (d) Summary data from flow cytometric analysis of spleens and peripheral blood following *i.v.* administration of Cre LNPs. Each stack of bars sums to the fraction of singlets classified as tdTomato$^+$ and is further stratified into distinct cell types. Statistical annotations above stacked bars indicate comparisons of total tdTomato expression in singlets. *: $p < 0.05$. **: $p < 0.01$. Statistical annotations without bars indicate comparisons to PBS. (e) Correlation analysis of high-throughput screening data *vs* validation study data for *i.v.* administration of LNP candidates. Data are presented as mean ± standard error of the mean for $4 \leq n \leq 6$ independent biological replicates.

regions. Generally, polyamine cores 482, 488, 494, and c494 showed strong delivery across multiple immune cell types and tissues. The 488, 494, and c494 polyamine cores have been previously reported by our group as promising candidates for immune cell transfection *in vitro* and *ex vivo*;[43,46] notably, however, the 482 core has previously demonstrated poor *in vitro* performance, making it a potential example of a false negative and demonstrating the value of multiplexed *in vivo* screening approaches.[43] Strikingly, the "gold standard" ionizable lipids C12−200 and MC3 generally showed relatively low delivery compared to our ionizable lipids, suggesting that these commonly used lipids may be relatively poorly suited to immune cell transfection following systemic administration.

Identification of mRNA LNPs for Potential Vaccine Applications. To confirm our high-throughput screening findings and evaluate the potential of our lead candidate LNPs for mRNA vaccine applications, we performed a validation study. Because mRNA vaccines require delivery of very little mRNA to very few APCs,[27,38] we sought to maximize the sensitivity of our validation study. To this end, we employed FLuc as a luminescence reporter gene to verify effective mRNA transfection. To study the effects of LNP composition on cellular uptake, we additionally tagged our LNPs with the lipophilic fluorescent dye 1,1′-dioctadecyl-3,3,3′,3′-tetramethylindodicarbocyanine (DiD) to facilitate flow cytometric analysis. We selected three LNPs identified by our high-

https://doi.org/10.1021/acsnano.4c01171
ACS Nano XXXX, XXX, XXX−XXX

throughput screening for validation experiments: LNP 7, formulated using the C12-200 ionizable lipid with nonstandard excipient composition (25.9% C12-200/21.6% DOPE/51.7% cholesterol/0.9% lipid-PEG); LNP 37, formulated using the ionizable lipid C16-488 (36.6% C16-488/6.1% DOPE/48.8% cholesterol/8.5% lipid-PEG); and LNP 39, formulated using the same lipid C16-488 but with substantially different excipient composition (25.9% C16-488/21.6% DOPE/51.7% cholesterol/0.9% lipid-PEG). LNPs 7 and 37 emerged from high-throughput screening as moderate and strong candidates, respectively, based on enrichment analysis, and were selected to evaluate the ability of our high-throughput screening methodology to predict relative LNP potency, while LNP 39 was a poor candidate and was selected to verify its status as a true negative (Figure 6b). In addition to these LNP formulations, we also tested an LNP using the clinical MC3 ionizable lipid (LNP 75) as a positive control. All LNPs tested in validation experiments were formulated containing only mRNA, *i.e.*, without b-DNA.

LNP 37 Demonstrates Enhanced Retention and Immune Transfection Compared to a Clinical Standard Ionizable Lipid. We administered DiD-tagged FLuc mRNA LNPs *via i.m.* injection to C57BL/6 mice and, after allowing time for LNPs to distribute and transfect cells, sacrificed the animals and performed *ex vivo* bioluminescence and fluorescence imaging to assess LNP transfection and accumulation, respectively (Figure 6a). LNPs 7, 37, and 75 all demonstrated substantial and indistinguishable FLuc expression in the draining lymph nodes, suggestive of successful transfection of resident immune cells (Figure 6c-d). Excitingly, LNP 37 demonstrated FLuc expression in the spleen at levels substantially exceeding any other condition tested—over an order-of-magnitude improvement in mean FLuc flux compared to the next-highest treatment group and roughly a 13-fold improvement in mean flux compared to the MC3 LNP. This enhanced splenic transfection has potential implications for *in vivo* immunoengineering due to the function of the spleen as a secondary lymphoid organ and the abundance of immunologically important cells in the spleen.[64,65] LNP 37 furthermore displayed significantly decreased FLuc expression in the liver compared with LNP 75 by approximately 4-fold. Conversely, LNP 39 demonstrated indistinguishable transfection from phosphate-buffered saline (PBS)-treated mice, confirming the ability of the high-throughput *in vivo* screening process to identify both strong and poor performers. Furthermore, our transfection results aligned well with the predictions from high-throughput screening: LNP 37, which demonstrated markedly greater enrichment than LNP 7 in both the spleen and lymph nodes, also demonstrated substantially greater mRNA transfection in validation experiments.

Analysis of LNP accumulation *via* DiD fluorescence was also performed. Notably, LNPs 7 and 37 both demonstrated substantially (roughly 3-fold and 4-fold, respectively) greater DiD fluorescence in the draining lymph nodes than LNP 75, which itself was indistinguishable from PBS (Figure 6e-f). LNP 39 did not display significantly different DiD fluorescence compared to PBS treatment. Surprisingly, LNP 37 was the only LNP formulation demonstrating a significant increase in DiD fluorescence in the liver compared with the PBS cohort. Flow cytometric analysis of cell-level LNP accumulation was generally consistent with organ imaging (Figure 6g): LNP 37 demonstrated significantly greater DiD positivity rates in the blood (8.6% ± 2.1% of singlets) compared to PBS (1.0% ± 0.2%) and LNPs 7 and 75 (1.6% ± 0.1% and 1.0% ± 0.1%, respectively), consistent with extravasation that could explain greater DiD signal in the liver. In the spleen, LNP 37 attained significantly greater DiD positivity rates (9.9% ± 1.7% of singlets) than any other treatment group, consistent with fluorescence images and demonstrating the potential of this LNP formulation for *in vivo* immunoengineering. Interestingly, LNP 37 displayed substantially greater tropism for B cells compared to other treatment groups, achieving approximately 4-fold greater mean accumulation in splenic B cells than the next-closest group and roughly 8-fold greater mean accumulation in splenic B cells than MC3. All told, validation experiments identified LNP 37 as a promising LNP formulation for potential use in applications, such as vaccines, that rely upon *i.m.* administration. The superior performance of LNP 37 to LNP 39—which uses the same C16–488 lipid but different excipient composition—further emphasizes the importance of lipid excipient composition on LNP fate under *i.m.* injection and the synergistic effects of ionizable lipid structure and excipient composition as identified by our high-throughput *in vivo* screening process.

Identification of LNPs for Potential Systemic Immunotherapies. To confirm our high-throughput screening findings and evaluate the potential of our lead candidate LNPs for extrahepatic *in vivo* immunoengineering, we performed another validation study. We employed an Ai9 (CAG-loxP-STOP-loxP-tdTomato) reporter mouse model in conjunction with the delivery of Cre mRNA for detection of mRNA translation on a single-cell level (Figure 7a). As with *i.m.* administration, we selected three LNPs for validation experiments: LNP 53, formulated using the C14–482 ionizable lipid; LNP 68, formulated using the C14-c494 ionizable lipid; and LNP 71, formulated using the C12–497 ionizable lipid. LNPs 53 and 68 were identified by enrichment analysis of high-throughput screening results as strong and moderate candidates, respectively, while LNP 71 was selected as a poor candidate (Figure 7b). In addition to these LNP formulations containing piperazine-derived ionizable lipids, we again tested LNP 75, which uses the clinical MC3 ionizable lipid, as a positive control.

C12-482 and C14-c494 LNPs Demonstrate Enhanced Transfection of Splenic and Circulating Leukocytes. 72 h following *i.v.* administration of LNPs encapsulating Cre mRNA to Ai9 mice, we sacrificed the animals and isolated spleens and peripheral blood, performing flow cytometric analysis to assess transfection efficiency in extrahepatic tissues. LNPs 53 and 68 demonstrated substantial and indistinguishable tdTomato expression (11.0% ± 1.7% and 9.1% ± 2.0% of singlets, respectively) in the blood (Figure 7c-d). Of particular note, LNP 53 displayed 5-fold greater transfection of circulating monocytes than any other LNP tested and roughly order-of-magnitude greater monocyte transfection than MC3. This potential for monocyte transfection is promising due to the potency of monocytes and monocyte-derived macrophages for immune polarization and potentiation.[66,67] LNP 71, identified by high-throughput screening as a poor candidate, demonstrated minimal transfection of circulating leukocytes and was indistinguishable (2.6% ± 1.2% tdTomato$^+$ singlets) from mice treated with either PBS (1.3% ± 0.3%) or the MC3-containing LNP 75 (2.8% ± 1.1%). In the spleen, however, only LNP 68 demonstrated significantly greater tdTomato expression (9.3% ± 2.9% of singlets) than PBS (1.1% ± 0.2%), also significantly outperforming LNPs 71 and 75 (1.3% ± 0.3% and 0.8% ± 0.1%, respectively). LNP 68 further displayed over 15-fold greater mean transfection of splenic DCs than the other LNPs tested—and nearly 50-fold greater mean splenic DC

https://doi.org/10.1021/acsnano.4c01171
ACS Nano XXXX, XXX, XXX−XXX

transfection than MC3. Altogether, LNPs 53 and 68 and their constituent ionizable lipids C14-482 and C14-c494 demonstrated significant promise for the transfection of circulating leukocytes under systemic administration, with LNP 68 also displaying its potential for the transfection of splenocytes, particularly splenic DCs.

Validation Experiments Confirm the Utility and Predictive Power of Multiplexed In Vivo Screening for Developing Immunotropic LNPs. While LNP internalization is necessary for mRNA transfection, it is not sufficient: endosomal escape represents a major barrier to LNP effectiveness.[20,68] We therefore anticipated the possibility for disparity between our high-throughput screening results, which reflect intracellular accumulation of LNP cargo, and actual functionality of LNPs, which requires effective endosomal escape. Therefore, having demonstrated the promise of our ionizable lipids for extrahepatic immune transfection for *in vivo* immunoengineering, we evaluated the performance of our high-throughput screening methodology itself. To this end, we investigated the relationship between high-throughput screening results, as summarized by normalized b-DNA accumulation, and low-throughput validation results, as summarized by tdTomato positivity rate (Figure 7e). Notably, nearly all cell types tested illustrated moderate positive correlation between predicted and actual performance, with the exception of peripheral T cells and both circulating and splenic DCs. It is possible that the immunobiology of T cells and DCs alters the efficacy of LNPs in manners not fully captured by analysis of b-DNA uptake. Previous studies have reported that endosomal acidification in T cells differs from other immune and nonimmune cells, which may lend this idea some credence.[69] Further work is needed to fully unravel the complex influences on LNP performance in these target cell types under systemic administration; however, we demonstrate a strong correlation between our high-throughput and validation results in B cells, macrophages, and monocytes, suggesting the suitability of high-throughput screening approaches for at least these target cell populations.

CONCLUSIONS

In vivo delivery of nucleoside-modified mRNA to immune cells holds great promise for immunoengineering, with applications in prophylactic vaccines, cancer immunotherapy, and beyond. LNPs have emerged as promising candidates for nucleic acid delivery, but structure−function relationships remain elusive, and their development is hindered by the limited throughput of typical *in vivo* screening methodologies. In this work, we employ high-throughput *in vivo* LNP screening based on molecular barcoding to identify key parameters influencing mRNA LNP immune transfection under both *i.m.* and *i.v.* administration and confirm the potential of lead LNP candidates for *in vivo* immunoengineering using mRNA. The information gleaned in this work provides critical insights into LNP design for immune transfection and the intricate interplay among administration route, ionizable lipid structure, and LNP composition in determining mRNA LNP efficacy and fate.

METHODS

Ionizable Lipid Synthesis. Ionizable lipids were synthesized by S_N2 reaction as described previously.[43] Briefly, polyamine cores (Figure S1) were reacted with alkyl epoxide tails containing 12, 14, or 16 carbons, with ethanol as a solvent, at 80 °C for 2 d. Reaction products were dried using a rotary evaporator and dissolved in ethanol at a known mass concentration for use in LNP synthesis. Ionizable lipid names are given as C<epoxide length>-<polyamine core number>. Polyamine core numbers c488 and c494 refer to the deoxygenated forms of the 488 and 494 cores, which differ only in the absence of ethers.

mRNA Synthesis. mRNA was synthesized *via in vitro* transcription (IVT) essentially as described previously.[46] FLuc or mCherry coding sequences (CDS) were cloned into an mRNA production plasmid with a 101 nt poly(A) tail. Sequences were transcribed with cotranscriptional capping using the CleanCap AG trinucleotide cap 1 analog, precipitated using lithium chloride, and purified using cellulose chromatography as described previously.[70] Uridine residues were fully substituted with N1-methylpseudouridine ($m^1\psi$). Resultant mRNA was analyzed by gel electrophoresis, sequenced, and checked for double-stranded RNA (dsRNA) contaminants using a J2 dot blot.

Cre recombinase IVT template was prepared by PCR amplification of gBlocks gene fragments containing a codon-optimized Cre recombinase CDS along with 5′ and 3′ untranslated regions (UTRs). Overhanging PCR primers were used to add a 100 nt poly(A) tail to the 3′ end of the IVT template. Sequences were transcribed with cotranscriptional capping using the CleanCap AG trinucleotide cap 1 analog, and mRNA transcripts were purified using solid-phase reversible immobilization (SPRI) beads. Uridine residues were fully substituted with $m^1\psi$, and 1 M urea was included as a chaotropic agent to reduce dsRNA formation.[71] mRNA integrity was confirmed *via* electrophoresis.

b-DNA Design. b-DNAs were designed as described previously.[53] Briefly, b-DNAs consisted of a 10 nt barcode region flanked by partial Illumina adapter sequences to allow for PCR-based ligation of NGS adapter and index sequences and to avoid differences in b-DNA sensitivity to exonuclease activity (Table S1). To minimize PCR bias and allow for read deduplication, b-DNAs also contained a 10 nt unique molecular identifier (UMI) sequence between the barcode sequence and 3′ flanking adapter sequence.

LNP Formulation. All LNPs studied were formulated *via* microfluidic mixing as described previously.[43] Briefly, all lipid components—ionizable lipid, DOPE, cholesterol, and C14-PEG2000—were prepared in ethanol, while all nucleic acids to be encapsulated were separately prepared in 10 mM citrate (pH 3). In all cases, the ratio of lipid to nucleic acid cargo was kept fixed and based on a prior high-throughput screening study.[72] The two phases were then combined at an aqueous:organic volume ratio of 3:1 in the channels of a microfluidic device with staggered herringbone microarchitecture to promote LNP self-assembly. After formulation, LNPs were dialyzed against 1× PBS for 2 h using a microdialysis well plate or dialysis cassettes (20 kDa MWCO).

LNP Characterization. *Size and Charge.* LNP size distributions were assessed in triplicate *via* dynamic light scattering (DLS) on a Zetasizer Nano following 100-fold dilution in 1× PBS. DLS measurements comprised 10 runs of 10 s with an initial equilibration period of 30 s. Zeta potential was measured in triplicate on a Zetasizer Nano following 50-fold dilution in water. Zeta potential measurements comprised at least 10 runs.

DNA Encapsulation. b-DNA encapsulation was assessed fluorometrically using the Quant-iT OliGreen reagent. A 3 μL aliquot of each LNP formulation was diluted 100-fold in 1× tris-EDTA (TE) buffer or 1× TE buffer containing 0.1% Triton X-100 surfactant. To avoid binding of probe reagent to mRNA, 1 μL of DNase-free RNase A was added to each sample and allowed to incubate at 25 °C. After 1 h of RNase incubation, 75 μL of each LNP dilution was plated in triplicate in black 96-well microplates. The OliGreen fluorescent probe reagent was diluted 200-fold in 1× TE buffer and 75 μL of diluted reagent was added to each well. After shaking and 5 min of incubation, fluorescence intensity was read on a Tecan Infinite 200 Pro microplate reader at an excitation wavelength of 480 nm and an emission wavelength of 520 nm.

RNA Encapsulation. mRNA encapsulation was assessed fluorometrically using the Quant-iT RiboGreen reagent. DNA digestion buffer was prepared as an aqueous solution of 20 mM tris-HCl, 10 mM $MgCl_2$, and 2 mM $CaCl_2$. A 3 μL aliquot of each LNP formulation was diluted 10-fold in DNA digestion buffer or DNA digestion buffer

https://doi.org/10.1021/acsnano.4c01171
ACS Nano XXXX, XXX, XXX−XXX

containing 1% Triton X-100 surfactant. To avoid binding of probe reagent to DNA, 1 U (0.5 μL) of RNase-free DNase I was added to each sample and allowed to incubate at 25 °C. After 90 min of DNase incubation, samples were further diluted 10-fold in 1× TE buffer to a final concentration of either 0% or 0.1% Triton X-100 for consistency with DNA encapsulation assays. 75 μL of each LNP dilution was plated in triplicate on black 96-well microplates. To enable RNA quantification, a 10-point standard curve of known RNA concentrations was also plated in duplicate on each plate. The RiboGreen fluorescent probe reagent was diluted 200-fold in 1× TE buffer and 75 μL of diluted reagent was added to each well. After shaking and 5 min of incubation, fluorescence intensity was read on a Tecan Infinite 200 Pro microplate reader at an excitation wavelength of 480 nm and an emission wavelength of 520 nm.

Animal Experiments. All animal use and experimental protocols were approved by the Institutional Animal Care and Use Committee (IACUC) at the University of Pennsylvania and followed guidelines set forth in the National Institutes of Health's Guide for the Care and Use of Laboratory Animals. Female C57BL/6 mice (initial screening) or Ai9 mice (counterscreening) were purchased from The Jackson Laboratory (Bay Harbor, ME) and housed in the Small Animal Imaging Facility at the University of Pennsylvania. For *i.m.* injection, 50 μL of LNP suspension was administered into each hind leg. For *i.v.* injection, 200 μL of LNP suspension was administered *via* the tail vein.

Primary Immune Cell Isolation. For analysis of circulating immune cells, peripheral blood was collected into microcentrifuge tubes pretreated with EDTA to prevent clotting. Lymph nodes were mechanically homogenized in microcentrifuge tubes to yield single-cell suspensions, while spleens were processed using 100 μm cell strainers. All samples containing red blood cells were rinsed several times with ammonium-chloride-potassium lysing buffer to lyse and remove red blood cells.

High-Throughput Screening of LNPs for Immune Cell Uptake. *Barcoded Oligomer Delivery and Cell Isolation.* For high-throughput screening, LNP formulations were combined in an equivolumic manner. This pool was used to inject C57BL/6 mice using *i.m.* or *i.v.* injections (n = 4 mice per administration route). 6 h (*i.v.*) or 12 h (*i.m.*) following injection, mice were sacrificed and blood, draining (inguinal) lymph nodes, and spleens were collected. Single-cell suspensions were then stained for FACS (see Figure S2). B cells, T cells, DCs, and macrophages/monocytes from each sample were sorted into DNA-stabilizing lysis buffer consisting of 100 mM tris, 5 mM EDTA, 200 mM sodium chloride, and 0.2% sodium dodecyl sulfate. A 100 μg portion of nuclease-free proteinase K and 12 μg of DNase-free RNase A were added to each sample and allowed to incubate overnight.

Barcoded Oligomer Isolation and Amplification. Following RNase and proteinase digestion, DNA oligomers were isolated from cell lysates using commercial centrifugal DNA cleanup columns according to the manufacturer's protocol. PCR was then performed to add sequencing adapters (P5 and P7) and indices (i7) to barcoded oligomers. The Phusion high-fidelity polymerase was used to perform 35 cycles of amplification with polymorphic overhanging primers containing adapters and indices. Following PCR, products were pooled and gel electrophoresis was performed on a 3% agarose gel to separate desired products from primer dimers and other undesired products. The 144 bp target band was excised from the gel and a gel extraction kit was used to isolate the PCR product.

NGS Library Pool Preparation and Sequencing. To construct a balanced pool, the double-stranded DNA (dsDNA) content of each band extracted following agarose gel electrophoresis was fluorometrically measured by using the Quant-iT PicoGreen reagent. Each sample was diluted 100-fold in 1× TE buffer and 100 μL of diluted sample was plated in a black 96-well microplate. To enable DNA quantification, a 10-point standard curve of known dsDNA concentrations was also plated. The PicoGreen fluorescent probe reagent was diluted 200-fold in 1× TE buffer and 100 μL of diluted reagent was added to each well. After shaking and 5 min of incubation, fluorescence intensity was read on a Tecan Infinite 200 Pro microplate reader at an excitation wavelength of 480 nm and an emission wavelength of 520 nm. 14 ng of each sample was combined to produce a balanced library pool for NGS. Quality control was performed on this library pool using an Agilent BioAnalyzer, and the pool was sequenced on an Illumina MiSeq using a 50 × 8 (read × index) geometry. The pool was loaded onto the flow cell at a 4 nM concentration.

NGS Data Analysis and Visualization. To analyze the next-generation sequencing data, a pipeline analogous to common single-cell sequencing techniques was developed and employed. Following demultiplexing, reads were trimmed of adapter sequences and matched to known barcode sequences using a program written in the Rust programming language. These barcode reads were then deduplicated by UMI, producing a count of unique molecules for each barcode within each sample. Read normalization was then performed by first dividing the deduplicated read count for each barcode by the sample grand total deduplicated read count (within-sample) and then dividing this quantity by the corresponding quantity in the samples corresponding to the uninjected pool (across-sample). The resultant quantity is referred to as "normalized accumulation" herein and reflects the relative prevalence of a given barcode in each experimental sample. Importantly, normalized accumulation cannot be directly compared across samples: it must be compared only within a sample (NGS library).

For statistical analysis of relative enrichment/depletion, Wilcoxon rank-sum tests were performed by comparing the normalized accumulation of each barcode against the normalized accumulation of all other barcodes within a sample (*i.e.*, basemean) using the normal approximation with continuity correction. Resultant p values were corrected for multiple comparisons using the false discovery rate method of Benjamini and Hochberg.[73]

To visualize the effects of excipient composition on relative delivery, bilinear interpolation was performed on the relevant explanatory variables (*i.e.*, excipient fractions), with normalized delivery as the response variable.[74] Data analysis and visualization were conducted using the R statistical programming language with a number of packages from the Comprehensive R Archive Network (CRAN).[75−91] Image transformation was assisted by the ImageMagick software.[92] The Nix package manager (with pinned `nixpkgs` revision `f44ba1b`) was used to manage all dependencies to maximize reproducibility.[93]

Validation of Lead LNP Candidates. *Intramuscular Administration.* For validation of lead LNP candidates for *i.m.* injection, luminescence measurements of transfection (to confirm potency) were used alongside fluorescence measurements of LNP accumulation (to validate NGS results). LNPs encapsulating mRNA encoding FLuc were formulated as described. Prior to administration, LNPs were dyed using the lipophilic fluorescent compound DiD at a concentration of 20 μM. C57BL/6 mice were injected in each hind leg with 3 μg of encapsulated mRNA in dyed LNPs. 12 h later, mice were given an intraperitoneal injection of 150 mg/kg of D-luciferin and sacrificed. After sacrifice, mouse organs and peripheral blood were collected. Organs were imaged for bioluminescence and DiD fluorescence using an *in vivo* imaging system (IVIS), and spleens and draining lymph nodes were reserved for flow cytometric analysis (Figure S3).

Intravenous Administration. For validation of lead LNP candidates for *i.v.* immune cell transfection, an Ai9 (CAG-loxP-STOP-loxP-tdTomato) mouse model was employed. LNPs encapsulating mRNA encoding Cre recombinase were formulated as described. Ai9 mice were injected at a dose of 0.8 mg/kg of encapsulated Cre mRNA. 72 h after injection, mice were sacrificed, and spleens and peripheral blood were collected and subjected to flow cytometric analysis (Figure S4).

FACS and Flow Cytometric Analysis. FACS was performed on either a BD FACSAria or a BD FACSJazz cell sorter, depending on instrument availability. In either case, cell sorters were equipped with ultraviolet, violet, blue, green, and red lasers. Flow cytometry was performed on a BD LSRII flow cytometer equipped with violet, blue, green, and red lasers. All antibodies used for fluorescence detection were obtained from BioLegend. Pacific Blue, FITC, PE, PE/cyanine 7, Brilliant Violet 650, and Alexa Fluor 700 were used as fluorophores; clones 17A2, M1/70, MB19-1, and Michel-19 were used for CD3, CD11b, CD19, and CD83, respectively. Data for compensation were acquired using singly stained controls, and fluorescence-minus-one (FMO) controls were employed as necessary to facilitate analysis.

https://doi.org/10.1021/acsnano.4c01171
ACS Nano XXXX, XXX, XXX−XXX

ASSOCIATED CONTENT

Supporting Information

The Supporting Information is available free of charge at https://pubs.acs.org/doi/10.1021/acsnano.4c01171.

LNP composition information, lists of b-DNA and primer sequences, chemical structures of polyamine cores used for ionizable lipid synthesis, and flow cytometry gating schemes (PDF)

AUTHOR INFORMATION

Corresponding Author

Michael J. Mitchell − *Department of Bioengineering, University of Pennsylvania, Philadelphia, Pennsylvania 19104, United States; Center for Precision Engineering for Health, University of Pennsylvania, Philadelphia, Pennsylvania 19104, United States; Institute for RNA Innovation, University of Pennsylvania, Philadelphia, Pennsylvania 19104, United States; Abramson Cancer Center, Perelman School of Medicine, University of Pennsylvania, Philadelphia, Pennsylvania 19104, United States; Center for Cellular Immunotherapies, Perelman School of Medicine, University of Pennsylvania, Philadelphia, Pennsylvania 19104, United States; Institute for Immunology, Perelman School of Medicine, University of Pennsylvania, Philadelphia, Pennsylvania 19104, United States; Cardiovascular Institute, Perelman School of Medicine, University of Pennsylvania, Philadelphia, Pennsylvania 19104, United States; Institute for Regenerative Medicine, Perelman School of Medicine, University of Pennsylvania, Philadelphia, Pennsylvania 19104, United States;* orcid.org/0000-0002-3628-2244; Email: mjmitch@seas.upenn.edu

Authors

Alex G. Hamilton − *Department of Bioengineering, University of Pennsylvania, Philadelphia, Pennsylvania 19104, United States;* orcid.org/0000-0002-9810-5630

Kelsey L. Swingle − *Department of Bioengineering, University of Pennsylvania, Philadelphia, Pennsylvania 19104, United States;* orcid.org/0000-0001-8475-9206

Ajay S. Thatte − *Department of Bioengineering, University of Pennsylvania, Philadelphia, Pennsylvania 19104, United States;* orcid.org/0000-0001-7372-8893

Alvin J. Mukalel − *Department of Bioengineering, University of Pennsylvania, Philadelphia, Pennsylvania 19104, United States*

Hannah C. Safford − *Department of Bioengineering, University of Pennsylvania, Philadelphia, Pennsylvania 19104, United States;* orcid.org/0000-0002-2512-8153

Margaret M. Billingsley − *Department of Bioengineering, University of Pennsylvania, Philadelphia, Pennsylvania 19104, United States;* orcid.org/0000-0003-4499-9066

Rakan D. El-Mayta − *Department of Bioengineering, University of Pennsylvania, Philadelphia, Pennsylvania 19104, United States*

Xuexiang Han − *Department of Bioengineering, University of Pennsylvania, Philadelphia, Pennsylvania 19104, United States*

Benjamin E. Nachod − *Department of Bioengineering, University of Pennsylvania, Philadelphia, Pennsylvania 19104, United States*

Ryann A. Joseph − *Department of Bioengineering, University of Pennsylvania, Philadelphia, Pennsylvania 19104, United States;* orcid.org/0000-0002-0795-6094

Ann E. Metzloff − *Department of Bioengineering, University of Pennsylvania, Philadelphia, Pennsylvania 19104, United States*

Complete contact information is available at: https://pubs.acs.org/10.1021/acsnano.4c01171

Notes

The authors declare the following competing financial interest(s): A.G.H., A.S.T., A.J.M., M.M.B., and M.J.M. are inventors on patent applications related to this work.

ACKNOWLEDGMENTS

The authors thank the Penn Cytomics and Cell Sorting Shared Resource Laboratory at the University of Pennsylvania (RRID: SCR_02376) and the Penn Genomics and Sequencing Core at the University of Pennsylvania (RRID: SCR_022382). M.J.M. acknowledges funding support from the National Institutes of Health (NIH) Director's New Innovator Award (DP2 TR002776), a National Science Foundation (NSF) CAREER Award (CBET-2145491), the Burroughs Wellcome Fund Career Award at the Scientific Interface, and the American Cancer Society (RGS-22-1122-01-ET). The authors thank the Weissman Lab at the University of Pennsylvania Perelman School of Medicine for providing some of the reporter mRNAs used in this study. A.G.H., K.L.S., A.S.T., A.J.M., H.C.S., and A.E.M. were supported by NSF Graduate Research Fellowships (award 1845298). M.M.B. was supported by an NIH F31 Fellowship (F31CA260922-03). This work is supported by Wellcome Leap as part of the R3 Program.

REFERENCES

(1) Neshat, S. Y.; Tzeng, S. Y.; Green, J. J. Gene delivery for immunoengineering. *Curr. Opin. Biotechnol.* **2020**, *66*, 1−10.

(2) Polack, F. P.; Thomas, S. J.; Kitchin, N.; Absalon, J.; Gurtman, A.; Lockhart, S.; Perez, J. L.; Pérez Marc, G.; Moreira, E. D.; Zerbini, C.; et al. Safety and Efficacy of the BNT162b2 mRNA Covid-19 Vaccine. *New England Journal of Medicine* **2020**, *383*, 2603−2615.

(3) Baden, L. R.; El Sahly, H. M.; Essink, B.; Kotloff, K.; Frey, S.; Novak, R.; Diemert, D.; Spector, S. A.; Rouphael, N.; Creech, C. B.; et al. Efficacy and Safety of the mRNA-1273 SARS-CoV-2 Vaccine. *New England Journal of Medicine* **2021**, *384*, 403−416.

(4) Ollmann Saphire, E. A. Vaccine against Ebola Virus. *Cell* **2020**, *181*, 6.

(5) Lundstrom, K. Viral Vectors for COVID-19 Vaccine Development. *Viruses* **2021**, *13*, 317.

(6) Cutrera, J.; King, G.; Jones, P.; Kicenuik, K.; Gumpel, E.; Xia, X.; Li, S. Safety and efficacy of tumor-targeted interleukin 12 gene therapy in treated and non-treated, metastatic lesions. *Current Gene Therapy* **2014**, *15*, 44−54.

(7) Sun, W.; Shi, Q.; Zhang, H.; Yang, K.; Ke, Y.; Wang, Y.; Qiao, L. Advances in the Techniques and Methodologies of Cancer Gene Therapy. *Discovery Medicine* **2019**, *27*, 45−55.

(8) Peng, M.; Mo, Y.; Wang, Y.; Wu, P.; Zhang, Y.; Xiong, F.; Guo, C.; Wu, X.; Li, Y.; Li, X.; et al. Neoantigen vaccine: an emerging tumor immunotherapy. *Molecular Cancer* **2019**, *18*, 128.

(9) Jogalekar, M. P.; Rajendran, R. L.; Khan, F.; Dmello, C.; Gangadaran, P.; Ahn, B.-C.; CAR, T. CAR T-Cell-Based gene therapy for cancers: new perspectives, challenges, and clinical developments. *Frontiers in Immunology* **2022**, *13*, 925985.

(10) Shafer, P.; Kelly, L. M.; Hoyos, V. Cancer Therapy With TCR-Engineered T Cells: Current Strategies, Challenges, and Prospects. *Frontiers in Immunology* **2022**, *13*, 835762.

(11) Yin, H.; Kanasty, R. L.; Eltoukhy, A. A.; Vegas, A. J.; Dorkin, J. R.; Anderson, D. G. Non-viral vectors for gene-based therapy. *Nat. Rev. Genet.* **2014**, *15*, 541−555.
(12) Shirley, J. L.; de Jong, Y. P.; Terhorst, C.; Herzog, R. W. Immune Responses to Viral Gene Therapy Vectors. *Molecular Therapy* **2020**, *28*, 709−722.
(13) Mohammadinejad, R.; Dehshahri, A.; Sagar Madamsetty, V.; Zahmatkeshan, M.; Tavakol, S.; Makvandi, P.; Khorsandi, D.; Pardakhty, A.; Ashrafizadeh, M.; Ghasemipour Afshar, E.; et al. In vivo gene delivery mediated by non-viral vectors for cancer therapy. *J. Controlled Release* **2020**, *325*, 249−275.
(14) Zu, H.; Gao, D. Non-viral Vectors in Gene Therapy: Recent Development, Challenges, and Prospects. *AAPS Journal* **2021**, *23*, 78.
(15) Bushman, F. D. Retroviral Insertional Mutagenesis in Humans: Evidence for Four Genetic Mechanisms Promoting Expansion of Cell Clones. *Molecular Therapy* **2020**, *28*, 352−356.
(16) FDA Investigating Serious Risk of T-cell Malignancy Following BCMA-Directed or CD19-Directed Autologous Chimeric Antigen Receptor (CAR) T cell Immunotherapies. https://www.fda.gov/vaccines-blood-biologics/safety-availability-biologics/fda-investigating-serious-risk-t-cell-malignancy-following-bcma-directed-or-cd19-directed-autologous (accessed Jan. 15, 2024).
(17) Namuduri, M.; Brentjens, R. J. Medical management of side effects related to CAR T cell therapy in hematologic malignancies. *Expert Review of Hematology* **2016**, *9*, 511−513.
(18) Ruella, M.; Xu, J.; Barrett, D. M.; Fraietta, J. A.; Reich, T. J.; Ambrose, D. E.; Klichinsky, M.; Shestova, O.; Patel, P. R.; Kulikovskaya, I.; et al. Induction of resistance to chimeric antigen receptor T cell therapy by transduction of a single leukemic B cell. *Nature Medicine* **2018**, *24*, 1499−1503.
(19) Karikó, K.; Muramatsu, H.; Welsh, F. A.; Ludwig, J.; Kato, H.; Akira, S.; Weissman, D. Incorporation of pseudouridine into mRNA yields superior nonimmunogenic vector with increased translational capacity and biological stability. *Molecular Therapy* **2008**, *16*, 1833−1840.
(20) Hamilton, A. G.; Swingle, K. L.; Mitchell, M. J. Biotechnology: Overcoming biological barriers to nucleic acid delivery using lipid nanoparticles. *PLOS Biology* **2023**, *21*, e3002105.
(21) Xu, S.; Yang, K.; Li, R.; Zhang, L. mRNA Vaccine Era−Mechanisms, Drug Platform and Clinical Prospection. *International Journal of Molecular Sciences* **2020**, *21*, 6582.
(22) Beck, J. D.; Reidenbach, D.; Salomon, N.; Sahin, U.; Tureci, O.; Vormehr, M.; Kranz, L. M. mRNA therapeutics in cancer immunotherapy. *Molecular Cancer* **2021**, *20*, 69.
(23) Liu, C.; Shi, Q.; Huang, X.; Koo, S.; Kong, N.; Tao, W. mRNA-based cancer therapeutics. *Nature Reviews Cancer* **2023**, *23*, 526−543.
(24) Chander, N.; Basha, G.; Yan Cheng, M. H.; Witzigmann, D.; Cullis, P. R. Lipid nanoparticle mRNA systems containing high levels of sphingomyelin engender higher protein expression in hepatic and extra-hepatic tissues. *Molecular Therapy. Methods & Clinical Development* **2023**, *30*, 235−245.
(25) Houseley, J.; Tollervey, D. The Many Pathways of RNA Degradation. *Cell* **2009**, *136*, 763−776.
(26) Reichmuth, A. M.; Oberli, M. A.; Jaklenec, A.; Langer, R.; Blankschtein, D. mRNA vaccine delivery using lipid nanoparticles. *Therapeutic Delivery* **2016**, *7*, 319−334.
(27) Sahin, U.; Karikó, K.; Tureci, O. mRNA-based therapeutics-developing a new class of drugs. *Nat. Rev. Drug Discovery* **2014**, *13*, 759−780.
(28) Kulkarni, J. A.; Myhre, J. L.; Chen, S.; Tam, Y. Y. C.; Danescu, A.; Richman, J. M.; Cullis, P. R. Design of lipid nanoparticles for in vitro and in vivo delivery of plasmid DNA. *Nanomedicine: Nanotechnology, Biology and Medicine* **2017**, *13*, 1377−1387.
(29) Guimaraes, L. C.; Costa, P. A. C.; Scalzo Júnior, S. R. A.; Ferreira, H. A. S.; Braga, A. C. S.; de Oliveira, L. C.; Figueiredo, M. M.; Shepherd, S.; Hamilton, A.; Queiroz-Junior, C. M.; et al. Nanoparticle-based DNA vaccine protects against SARS-CoV-2 variants in female preclinical models. *Nat. Commun.* **2024**, *15*, 590.
(30) Yang, L.; Ma, F.; Liu, F.; Chen, J.; Zhao, X.; Xu, Q. Efficient Delivery of Antisense Oligonucleotides Using Bioreducible Lipid Nanoparticles In Vitro and In Vivo. *Molecular Therapy - Nucleic Acids* **2020**, *19*, 1357−1367.
(31) Love, K. T.; Mahon, K. P.; Levins, C. G.; Whitehead, K. A.; Querbes, W.; Dorkin, J. R.; Qin, J.; Cantley, W.; Qin, L. L.; Racie, T.; et al. Lipid-like materials for low-dose, in vivo gene silencing. *Proc. Natl. Acad. Sci. U. S. A.* **2010**, *107*, 1864−1869.
(32) Billingsley, M. M.; Hamilton, A. G.; Mai, D.; Patel, S. K.; Swingle, K. L.; Sheppard, N. C.; June, C. H.; Mitchell, M. J. Orthogonal Design of Experiments for Optimization of Lipid Nanoparticles for mRNA Engineering of CAR T Cells. *Nano Lett.* **2022**, *22*, 533−542.
(33) Eygeris, Y.; Gupta, M.; Kim, J.; Sahay, G. Chemistry of Lipid Nanoparticles for RNA Delivery. *Acc. Chem. Res.* **2022**, *55*, 2−12.
(34) Swingle, K. L.; Hamilton, A. G.; Mitchell, M. J. Lipid Nanoparticle-Mediated Delivery of mRNA Therapeutics and Vaccines. *Trends in Molecular Medicine* **2021**, *27*, 616−617.
(35) Cheng, Q.; Wei, T.; Farbiak, L.; Johnson, L. T.; Dilliard, S. A.; Siegwart, D. J. Selective ORgan Targeting (SORT) nanoparticles for tissue specific mRNA delivery and CRISPR/Cas gene editing. *Nat. Nanotechnol.* **2020**, *15*, 313−320.
(36) Swingle, K. L.; Safford, H. C.; Geisler, H. C.; Hamilton, A. G.; Thatte, A. S.; Billingsley, M. M.; Joseph, R. A.; Mrksich, K.; Padilla, M. S.; Ghalsasi, A. A.; et al. Ionizable Lipid Nanoparticles for In Vivo mRNA Delivery to the Placenta during Pregnancy. *J. Am. Chem. Soc.* **2023**, *145*, 4691−4706.
(37) Melamed, J. R.; Hajj, K. A.; Chaudhary, N.; Strelkova, D.; Arral, M. L.; Pardi, N.; Alameh, M.-G.; Miller, J. B.; Farbiak, L.; Siegwart, D. J.; et al. Lipid nanoparticle chemistry determines how nucleoside base modifications alter mRNA delivery. *J. Controlled Release* **2022**, *341*, 206−214.
(38) Pardi, N.; Hogan, M. J.; Porter, F. W.; Weissman, D. mRNA vaccines − a new era in vaccinology. *Nat. Rev. Drug Discovery* **2018**, *17*, 261−279.
(39) Mukalel, A. J.; Riley, R. S.; Zhang, R.; Mitchell, M. J. Nanoparticles for Nucleic Acid Delivery: Applications in Cancer Immunotherapy. *Cancer Letters* **2019**, *458*, 102−112.
(40) Akinc, A.; Zumbuehl, A.; Goldberg, M.; Leshchiner, E. S.; Busini, V.; Hossain, N.; Bacallado, S. A.; Nguyen, D. N.; Fuller, J.; Alvarez, R.; et al. A combinatorial library of lipid-like materials for delivery of RNAi therapeutics. *Nat. Biotechnol.* **2008**, *26*, 561−569.
(41) Jayaraman, M.; Ansell, S. M.; Mui, B. L.; Tam, Y. K.; Chen, J.; Du, X.; Butler, D.; Eltepu, L.; Matsuda, S.; Narayanannair, J. K.; et al. Maximizing the potency of siRNA lipid nanoparticles for hepatic gene silencing in vivo. *Angewandte Chemie (International Ed. in English)* **2012**, *51*, 8529−8533.
(42) Lin, P. J. C.; Tam, Y. Y. C.; Hafez, I.; Sandhu, A.; Chen, S.; Ciufolini, M. A.; Nabi, I. R.; Cullis, P. R. Influence of cationic lipid composition on uptake and intracellular processing of lipid nanoparticle formulations of siRNA. *Nanomedicine: Nanotechnology, Biology and Medicine* **2013**, *9*, 233−246.
(43) Billingsley, M. M.; Singh, N.; Ravikumar, P.; Zhang, R.; June, C. H.; Mitchell, M. J. Ionizable Lipid Nanoparticle-Mediated mRNA Delivery for Human CAR T Cell Engineering. *Nano Lett.* **2020**, *20*, 1578−1589.
(44) Xue, L.; Gong, N.; Shepherd, S. J.; Xiong, X.; Liao, X.; Han, X.; Zhao, G.; Song, C.; Huang, X.; Zhang, H.; et al. Rational Design of Bisphosphonate Lipid-like Materials for mRNA Delivery to the Bone Microenvironment. *J. Am. Chem. Soc.* **2022**, *144*, 9926−9937.
(45) Kauffman, K. J.; Dorkin, J. R.; Yang, J. H.; Heartlein, M. W.; DeRosa, F.; Mir, F. F.; Fenton, O. S.; Anderson, D. G. Optimization of Lipid Nanoparticle Formulations for mRNA Delivery in Vivo with Fractional Factorial and Definitive Screening Designs. *Nano Lett.* **2015**, *15*, 7300−7306.
(46) Hamilton, A. G.; Swingle, K. L.; Joseph, R. A.; Mai, D.; Gong, N.; Billingsley, M. M.; Alameh, M.-G.; Weissman, D.; Sheppard, N. C.; June, C. H.; Mitchell, M. J.; et al. Ionizable Lipid Nanoparticles with Integrated Immune Checkpoint Inhibition for mRNA CAR T Cell Engineering. *Adv. Healthcare Mater.* **2023**, *12*, 2301515.

https://doi.org/10.1021/acsnano.4c01171
ACS Nano XXXX, XXX, XXX−XXX

(47) Swingle, K. L.; Billingsley, M. M.; Bose, S. K.; White, B.; Palanki, R.; Dave, A.; Patel, S. K.; Gong, N.; Hamilton, A. G.; Alameh, M.-G.; et al. Amniotic fluid stabilized lipid nanoparticles for in utero intra-amniotic mRNA delivery. *J. Controlled Release* **2022**, *341*, 616−633.
(48) Eygeris, Y.; Patel, S.; Jozic, A.; Sahay, G. Deconvoluting Lipid Nanoparticle Structure for Messenger RNA Delivery. *Nano Lett.* **2020**, *20*, 4543−4549.
(49) Whitehead, K. A.; Dorkin, J. R.; Vegas, A. J.; Chang, P. H.; Veiseh, O.; Matthews, J.; Fenton, O. S.; Zhang, Y.; Olejnik, K. T.; Yesilyurt, V.; et al. Degradable lipid nanoparticles with predictable in vivo siRNA delivery activity. *Nat. Commun.* **2014**, *5*, 4277.
(50) Fenton, O. S.; Kauffman, K. J.; McClellan, R. L.; Kaczmarek, J. C.; Zeng, M. D.; Andresen, J. L.; Rhym, L. H.; Heartlein, M. W.; DeRosa, F.; Anderson, D. G. Customizable Lipid Nanoparticle Materials for the Delivery of siRNAs and mRNAs. *Angew. Chem., Int. Ed.* **2018**, *57*, 13582−13586.
(51) Dahlman, J. E.; Kauffman, K. J.; Xing, Y.; Shaw, T. E.; Mir, F. F.; Dlott, C. C.; Langer, R.; Anderson, D. G.; Wang, E. T. Barcoded nanoparticles for high throughput in vivo discovery of targeted therapeutics. *Proc. Natl. Acad. Sci. U. S. A.* **2017**, *114*, 2060−2065.
(52) Lokugamage, M. P.; Sago, C. D.; Gan, Z.; Krupczak, B. R.; Dahlman, J. E. Constrained nanoparticles deliver siRNA and sgRNA to T cells in vivo without targeting ligands. *Adv. Mater.* **2019**, *31*, e1902251.
(53) El-Mayta, R.; Zhang, R.; Shepherd, S. J.; Wang, F.; Billingsley, M. M.; Dudkin, V.; Klein, D.; Lu, H. D.; Mitchell, M. J. A Nanoparticle Platform for Accelerated In Vivo Oral Delivery Screening of Nucleic Acids. *Advanced Therapeutics* **2021**, *4*, 2000111.
(54) Guimaraes, P. P. G.; Zhang, R.; Spektor, R.; Tan, M.; Chung, A.; Billingsley, M. M.; El-Mayta, R.; Riley, R. S.; Wang, L.; Wilson, J. M.; et al. Ionizable lipid nanoparticles encapsulating barcoded mRNA for accelerated in vivo delivery screening. *J. Controlled Release* **2019**, *316*, 404−417.
(55) Pardi, N.; Tuyishime, S.; Muramatsu, H.; Kariko, K.; Mui, B. L.; Tam, Y. K.; Madden, T. D.; Hope, M. J.; Weissman, D. Expression kinetics of nucleoside-modified mRNA delivered in lipid nanoparticles to mice by various routes. *J. Controlled Release* **2015**, *217*, 345−351.
(56) Tsoi, K. M.; MacParland, S. A.; Ma, X.-Z.; Spetzler, V. N.; Echeverri, J.; Ouyang, B.; Fadel, S. M.; Sykes, E. A.; Goldaracena, N.; Kaths, J. M.; et al. Mechanism of hard-nanomaterial clearance by the liver. *Nat. Mater.* **2016**, *15*, 1212−1221.
(57) Zhang, R.; El-Mayta, R.; Murdoch, T. J.; Warzecha, C. C.; Billingsley, M. M.; Shepherd, S. J.; Gong, N.; Wang, L.; Wilson, J. M.; Lee, D.; et al. Helper lipid structure influences protein adsorption and delivery of lipid nanoparticles to spleen and liver. *Biomaterials Science* **2021**, *9*, 1449−1463.
(58) Ferraresso, F.; Strilchuk, A. W.; Juang, L. J.; Poole, L. G.; Luyendyk, J. P.; Kastrup, C. J. Comparison of DLin-MC3-DMA and ALC-0315 for siRNA Delivery to Hepatocytes and Hepatic Stellate Cells. *Mol. Pharmaceutics* **2022**, *19*, 2175−2182.
(59) Xu, X.; Wang, X.; Liao, Y.-P.; Luo, L.; Xia, T.; Nel, A. E. Use of a Liver-Targeting Immune-Tolerogenic mRNA Lipid Nanoparticle Platform to Treat Peanut-Induced Anaphylaxis by Single- and Multiple-Epitope Nucleotide Sequence Delivery. *ACS Nano* **2023**, *17*, 4942−4957.
(60) Paunovska, K.; Sago, C. D.; Monaco, C. M.; Hudson, W. H.; Castro, M. G.; Rudoltz, T. G.; Kalathoor, S.; Vanover, D. A.; Santangelo, P. J.; Ahmed, R.; et al. A direct comparison of in vitro and in vivo nucleic acid delivery mediated by hundreds of nanoparticles reveals a weak correlation. *Nano Lett.* **2018**, *18*, 2148−2157.
(61) Bashiri, G.; Padilla, M. S.; Swingle, K. L.; Shepherd, S. J.; Mitchell, M. J.; Wang, K. Nanoparticle protein corona: from structure and function to therapeutic targeting. *Lab Chip* **2023**, *23*, 1432−1466.
(62) Chen, D.; Ganesh, S.; Wang, W.; Amiji, M. The role of surface chemistry in serum protein corona-mediated cellular delivery and gene silencing with lipid nanoparticles. *Nanoscale* **2019**, *11*, 8760−8775.
(63) Francia, V.; Schiffelers, R. M.; Cullis, P. R.; Witzigmann, D. The Biomolecular Corona of Lipid Nanoparticles for Gene Therapy. *Bioconjugate Chem.* **2020**, *31*, 2046−2059.
(64) Kranz, L. M.; Diken, M.; Haas, H.; Kreiter, S.; Loquai, C.; Reuter, K. C.; Meng, M.; Fritz, D.; Vascotto, F.; Hefesha, H.; et al. Systemic RNA delivery to dendritic cells exploits antiviral defence for cancer immunotherapy. *Nature* **2016**, *534*, 396−401.
(65) Nakamura, T.; Sato, Y.; Yamada, Y.; Abd Elwakil, M. M.; Kimura, S.; Younis, M. A.; Harashima, H. Extrahepatic targeting of lipid nanoparticles in vivo with intracellular targeting for future nanomedicines. *Adv. Drug Delivery Rev.* **2022**, *188*, 114417.
(66) Gong, N.; Han, X.; Xue, L.; El-Mayta, R.; Metzloff, A. E.; Billingsley, M. M.; Hamilton, A. G.; Mitchell, M. J. In situ PEGylation of CAR T cells alleviates cytokine release syndrome and neurotoxicity. *Nat. Mater.* **2023**, *22*, 1571−1580.
(67) Sloas, C.; Gill, S.; Klichinsky, M. Engineered CAR-Macrophages as Adoptive Immunotherapies for Solid Tumors. *Frontiers in Immunology* **2021**, *12*, 783305.
(68) Chatterjee, S.; Kon, E.; Sharma, P.; Peer, D. Endosomal escape: A bottleneck for LNP-mediated therapeutics. *Proc. Natl. Acad. Sci. U. S. A.* **2024**, *121*, e2307800120.
(69) Olden, B. R.; Cheng, E.; Cheng, Y.; Pun, S. H. Identifying key barriers in cationic polymer gene delivery to human T cells. *Biomaterials Science* **2019**, *7*, 789−797.
(70) Baiersdörfer, M.; Boros, G.; Muramatsu, H.; Mahiny, A.; Vlatkovic, I.; Sahin, U.; Karikó, K. A Facile Method for the Removal of dsRNA Contaminant from In Vitro-Transcribed mRNA. *Molecular Therapy - Nucleic Acids* **2019**, *15*, 26−35.
(71) Piao, X.; Yadav, V.; Wang, E.; Chang, W.; Tau, L.; Lindenmuth, B. E.; Wang, S. X. Double-stranded RNA reduction by chaotropic agents during in vitro transcription of messenger RNA. *Molecular Therapy - Nucleic Acids* **2022**, *29*, 618−624.
(72) Sago, C. D.; Lokugamage, M. P.; Paunovska, K.; Vanover, D. A.; Monaco, C. M.; Shah, N. N.; Gamboa Castro, M.; Anderson, S. E.; Rudoltz, T. G.; Lando, G. N.; et al. High-throughput in vivo screen of functional mRNA delivery identifies nanoparticles for endothelial cell gene editing. *Proc. Natl. Acad. Sci. U. S. A.* **2018**, *115*, E9944−E9952.
(73) Benjamini, Y.; Hochberg, Y. Controlling the False Discovery Rate: A Practical and Powerful Approach to Multiple Testing. *J. Royal Stat. Soc. Ser. B (Methodological)* **1995**, *57*, 289−300.
(74) Akima, H. Algorithm 761: Scattered-data surface fitting that has the accuracy of a cubic polynomial. *ACM Transactions on Mathematical Software* **1996**, *22*, 362−371.
(75) R Core Team. *R*, version 4.2.1; 2022.
(76) Robinson, D.; Hayes, A.; Couch, S. *broom*, version 1.0.0; 2022.
(77) Wickham, H.; François, R.; Henry, L.; Müller, K. *dplyr*, version 1.0.9; 2022.
(78) Wickham, H. *forcats*, version 0.5.1; 2021.
(79) Clarke, E.; Sherrill-Mix, S. *ggbeeswarm*, version 0.6.0; 2017.
(80) Wickham, H. *ggplot2: Elegant Graphics for Data Analysis*; Springer-Verlag: New York, 2016.
(81) Aphalo, P. J. *ggpmisc*, version 0.5.0; 2022.
(82) Slowikowski, K. *ggrepel*, version 0.9.1; 2021.
(83) Auguie, B. *gridExtra*, version 2.3; 2017.
(84) Gebhardt, A.; Bivand, R.; Sinclair, D. *interp*, version 1.1−3; 2022.
(85) Greenwell, B. M.; Kabban, C. M. S. investr: An R Package for Inverse Estimation. *R Journal* **2014**, *6*, 90−100.
(86) Ooms, J. *magick*, version 2.7.3; 2021.
(87) Pedersen, T. L. *patchwork*, version 1.1.1; 2020.
(88) Wickham, H.; Hester, J.; Bryan, J. *readr*, version 2.1.2; **2022**.
(89) Wickham, H.; Bryan, J. *readxl*, version 1.4.0; 2022.
(90) Wickham, H. *stringr*, version 1.4.0; 2019.
(91) Wickham, H.; Girlich, M. *tidyr*, version 1.2.0; 2022.
(92) ImageMagick Studio LLC. *ImageMagick*, version 7.1.1−19; 2023.
(93) Dolstra, E. *The purely functional software deployment model*. 2006; https://dspace.library.uu.nl/handle/1874/7540 (accessed Jan. 29, 2024).

https://doi.org/10.1021/acsnano.4c01171
ACS Nano XXXX, XXX, XXX−XXX